Master thesis

Czech Technical University in Prague

F3 Faculty of Electrical Engineering
Department of Electromagnetic Field

Shape synthesis based on exact reanalysis

Jonáš Tuček

Supervisor: doc. Ing. Miloslav Čapek, Ph.D.
Supervisor–specialist: doc. Ing. Lukáš Jelínek, Ph.D.
Field of study: Electronics and Communications
Subfield: Radio systems
May 2021

ZADÁNÍ DIPLOMOVÉ PRÁCE

I. OSOBNÍ A STUDIJNÍ ÚDAJE

Příjmení: **Tuček** Jméno: **Jonáš** Osobní číslo: **466239**

Fakulta/ústav: **Fakulta elektrotechnická**

Zadávající katedra/ústav: **Katedra elektromagnetického pole**

Studijní program: **Elektronika a komunikace**

Specializace: **Rádiové komunikace a systémy**

II. ÚDAJE K DIPLOMOVÉ PRÁCI

Název diplomové práce:

Tvarová syntéza založená na perturbaci přesných modelů

Název diplomové práce anglicky:

Shape synthesis based on exact reanalysis

Pokyny pro vypracování:

Study the initial proposal of exact reanalysis procedure based on perturbation of impedance operator represented by piecewise-defined basis functions [1]. Compare the method with other optimization algorithms, namely, with topology optimization [2], heuristic algorithms [3], and surrogate models [4]. Discuss their similarities and differences. Identify properties and features of these methods that might be imported into the exact reanalysis procedure, e.g., restart based on heuristics or simplification based on surrogate models.
Generalize the original formulation to be able to operate over basis functions as well as over discretization elements. Compare these two approaches focusing on physical interpretation, computational burden, and manufacturing aspects. Adapt the matrix inversion based on Sherman-Morrison-Woodbury identity [5] to MATLAB-based vectorization. Utilize a heuristic scheme [6] to restart the local search when stuck in a local minimum.
Verify the functionality of the implemented procedure optimizing selected antenna metrics (e.g., maximal bandwidth, …). Compare the performance of the method with known realizations based on topology optimization [7].
Identify and discuss the framework's weaknesses and propose improvements that make the procedure viable for realistic antenna design.

Seznam doporučené literatury:

[1] Capek, M., Jelinek, L., Gustafsson, M.: Inversion-Free Evaluation of Nearest Neighbors in Method of Moments, IEEE Antennas Wireless Propag. Lett., Vol. 18, pp. 2311-2315, 2019.
[2] Bendsoe, M. P., Sigmund, O.: Topology Optimization Springer, Springer, 2004.
[3] Rahmat-Samii, Y. (Ed.), Michielssen, E. (Ed.): Electromagnetic Optimization by Genetic Algorithms, Wiley, 1999.
[4] Koziel, S., Ogurtsov, S.: Antenna Design by Simulation-Driven Optimization, Springer, 2014.
[5] Hager, W. W.: Updating the Inverse of a Matrix, SIAM Review, Vol. 31, pp. 221-239, 1989.
[6] Deb, K.: Multi-Objective Optimization using Evolutionary Algorithms, Wiley, 2001.
[7] Liu, S., Wang, Q., Gao, R.: MoM-based topology optimization method for planar metallic antenna design, Acta Mech. Sin., Vol 32, No. 6, pp. 1058-1064, 2016.

Jméno a pracoviště vedoucí(ho) diplomové práce:

doc. Ing. Miloslav Čapek, Ph.D., katedra elektromagnetického pole FEL

Jméno a pracoviště druhé(ho) vedoucí(ho) nebo konzultanta(ky) diplomové práce:

Datum zadání diplomové práce: **09.02.2021** Termín odevzdání diplomové práce: _____

Platnost zadání diplomové práce: **30.09.2022**

_____ _____ _____
doc. Ing. Miloslav Čapek, Ph.D. podpis vedoucí(ho) ústavu/katedry prof. Mgr. Petr Páta, Ph.D.
podpis vedoucí(ho) práce   podpis děkana(ky)

III. PŘEVZETÍ ZADÁNÍ

Diplomant bere na vědomí, že je povinen vypracovat diplomovou práci samostatně, bez cizí pomoci, s výjimkou poskytnutých konzultací.
Seznam použité literatury, jiných pramenů a jmen konzultantů je třeba uvést v diplomové práci.

.
_____
Datum převzetí zadání

_____
Podpis studenta

Acknowledgements

Declaration

I hereby declare that I have completed this thesis individually and that I have listed all used information sources in accordance with "Metodický pokyn o dodržování etických principů při přípravě vysokoškolských závěrečných prací".

In Prague, the 21. May 2021

Abstract

A topology optimization technique based on a mesh element perturbation scheme is proposed within method-of-moments formalism. The procedure is based on an inversion-free evaluation of topological sensitivities, constituting a gradient-based local step that is iteratively restarted by the genetic algorithm. The developed algorithm is compared to the existing algorithm, implemented in Antenna Toolbox for MATLAB, based on a single basis function removal. The method's validity and effectiveness are demonstrated in a variety of examples. The developed method is also compared to the known realizations based on the adjoint formulation of topology optimization. The viability of the proposed optimization procedure is also demonstrated by manufacturing two obtained designs.

Keywords: Antenna synthesis, Sherman-Morrison-Woodbury identity, topology sensitivity.

Supervisor: doc. Ing. Miloslav Čapek, Ph.D.

Abstrakt

V rámci formalismu metody momentů je navržena technika topologické optimalizace s blokovým poruchovým schématem. Procedura je založena na vyhodnocení topologické citlivosti bez nutnosti opakované maticové inverze. Lokální krok je iterativně restartován genetickým optimalizátorem. Vyvinutý algoritmus je porovnán s již existujícím algoritmem, implementovaným v anténním toolboxu AToM vyvíjeném v postředí MATLAB, založeným na strukturální modifikaci na úrovni bázových funkcí. Vlastnosti metody jsou ověřeny v sérii příkladů s důrazem na realizované hodnoty fyzikálních kvantit a výpočetní náročnost. Metoda je rovněž porovnána se známými realizacemi založenými na adjoint formulaci topologické optimalizace. Funkčnost navrženého optimalizačního postupu je rovněž demonstrována výrobou dvou získaných návrhů.

Klíčová slova: Syntéza antén, Sherman-Morrison-Woodbury identita, topologická citlivost.

Překlad názvu: Tvarová syntéza založená na perturbaci přesných modelů

Contents

Figures

x

xi

Tables

Chapter 1

Introduction

Wireless communication systems have become inseparable parts of our every-day life. One cannot simply imagine living without wireless devices such as smartphones, which worldwide quantity is immense and is inevitably growing. According to Cisco forecast [1], the ever-changing mix and growth of wireless devices that are accessing mobile networks worldwide are among the primary contributors to global mobile data traffic growth. Globally, mobile devices are predicted to reach 12.3 billion by 2022. The number of devices is closely interrelated with the mobile data traffic, which is expected to grow to 77 exabytes (10^{18} bytes) per month by 2022, a seven-fold increase as compared to 2017, see figure 1.1. Evolution towards more ingenious devices inevitably leads to more restrictive demands, which require optimized communication devices with a primal focus on high data rate, small size, and power efficiency.

(a) : Global mobile data traffic growth. **(b) :** Global mobile devices growth.
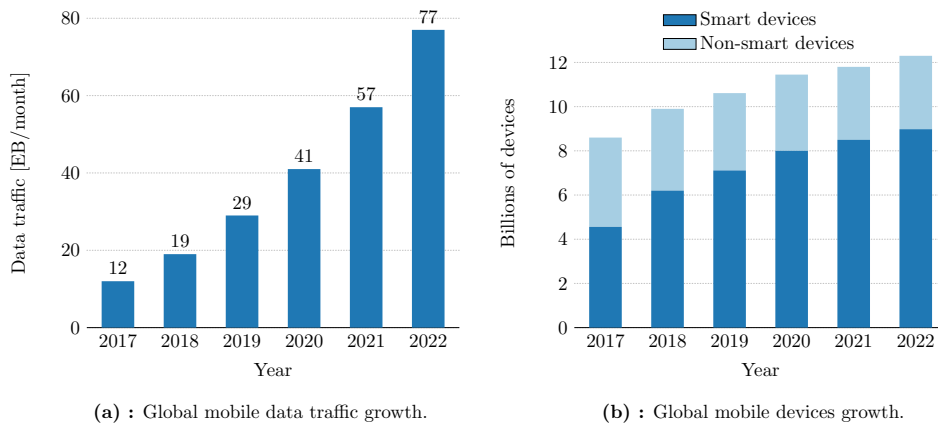
Figure 1.1: Cisco's annual internet report predicts the assessment of digital transformation across various business segments. The left and the right figure presents the overall growth rate of mobile data traffic per month and the total number of mobile devices, respectively (data taken from [1]). We define *smart devices* as those having advanced computing and multimedia capabilities with a minimum of 3G connectivity.

Antennas are inevitable parts of every wireless communication systems, *e.g.*, smartphones, radio frequency identification tags (RFID) or navigation systems (GPS). They must comply with prescribed performance require-

ments, *e.g.*, low return loss, wide bandwidth and good antenna gain. With the increasing number of communication channels, there is a growing demand for designing compact antennas in mobile communication. However, the antennas' performance is affected by miniaturization, and many of the existing requirements are then beyond the reach of empirical design procedures. Therefore, achieving miniaturization with satisfactory antenna performance is a challenging task. These demands force antenna designers to look for unconventional designs, often found via numerical optimization.

The design of an electromagnetic radiator is a difficult problem, often composed of two steps: *synthesis* and *analysis* [2], see figure 1.2 for an illustration.

An electromagnetic analysis specifies the geometrical shape, including material distribution and feeding position, then determines an unknown state variable that fully describes the state of a structure, *e.g.*, current density or electric field. The state variable is further used to evaluate the performance metrics. A skilled engineer often knows how to design a shape of a radiator and its material distribution to fulfil performance requirements due to his previous experience with similar antennas. If the conditions are not satisfied, he somehow modifies the geometry and analyzes it once again. Hence, the classical antenna design is an iterative and time-consuming process that handicaps unskilled designers. Nevertheless, the analysis has already been mastered thanks to modern computational methods [3], and many advanced electromagnetic simulators exist, *e.g.*, FEKO [4] or CST Studio Suite [5].
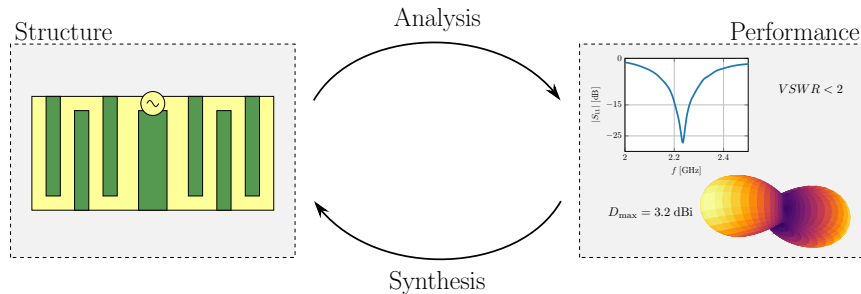
Figure 1.2: A comparison of antenna analysis and synthesis. The most important difference between the two is the non-uniqueness and NP-hardness [6] of the synthesis problem.

An antenna synthesis attempts to find the optimal geometrical shape of the radiator, material distribution and feeding network for given performance requirements. Despite a considerable theoretical development in computer science [7] and optimization theory [8], the problem of synthesis is far from being mastered. Theoretically, the main problem is an infinite number of degrees of freedom since the performance requirement may be accomplished by almost any shape. The problem of antenna synthesis is recognized as non-polynomial in time (NP) [6], and the underlying solution algorithms suffer from the curse of dimensionality [9].

In the current state of the art, the most successful treatments of the syn-

thesis problem are parametric sweeps, surrogate-based optimization [10], topology optimization [11] and shape optimization based on exact re-analysis [12]. In fact, these approaches employ a repetitive analysis and are typically connected to heuristic optimization algorithms [13].

This thesis is highly motivated by a topology sensitivity algorithm based on exact re-analysis [12] and its fundamental interpretation issue: removal of a single edge does not have a simple geometrical interpretation. Therefore, this thesis aims to develop a similar algorithm within method of moments paradigm [14] with a block perturbation scheme, since a removal of a block, *e.g.*, discretization element, is easily interpreted in terms of geometrical modification. Functionality and feasibility of developed procedures in the field of antenna synthesis are demonstrated in several examples.

Chapter 2

Antenna design

This chapter briefly introduces analysis and synthesis techniques and presents their interconnection. Afterwards, the solution methods for handling developed optimization tasks and the most successful treatments of the synthesis problem are presented in subsequent sections.

Let the antenna analysis be denoted as a process $\mathcal{A}$, which is an inseparable part of the antenna design task and may be formulated as follows: An incident field $\boldsymbol{E}^{\mathrm{i}}$ excites an electromagnetic structure with a fixed shape and material distribution Ω, and the goal is to evaluate electromagnetic or geometric performance metrics $\boldsymbol{p}$

$$\mathcal{A}\left\{\Omega, \boldsymbol{E}^{\mathrm{i}}\right\} = \begin{pmatrix} p_1 \\ \vdots \\ p_N \end{pmatrix}, \tag{2.1}$$

where N is the total number of metrics to be evaluated. Process of analysis $\mathcal{A}$ must necessarily contain a governing equation, a mathematical prescription of the physical behavior of the system, in the form of integro-differential equations stemming from Maxwell's equations.

Simple geometries may be solved by analytical methods [3], but arbitrary shaped bodies are solved by computational methods by introducing discretization to the problem. Finite difference methods, *e.g.*, Finite-Difference Time-Domain method (FDTD) [15], employs the spatial domain and time interval discretization, and the solution value is determined at these discrete points by solving algebraic equations containing finite differences. However, variational methods [3], used in this thesis, leads to a system of linear equations by expanding the state variable into a set of basis functions, which accurately model the unknown field distribution and offers flexibility in describing complex shapes. This is the main idea behind finite element method (FEM) [16] and method of moments (MoM) [14], two leading schemes in computational electromagnetics of time-harmonic fields[1].

The synthesis task is formulated as an inverse to the analysis

$$\{\Omega, \boldsymbol{E}^{\mathrm{i}}\} = \mathcal{A}^{-1}\boldsymbol{p} = \mathcal{S}\boldsymbol{p}_{\mathrm{user}}, \tag{2.2}$$

---

[1]MoM was also employed on EFIE in time-domain [17].

where solution $\{\Omega, \boldsymbol{E}^{\mathrm{i}}\}$ is non-unique. Figure 2.1 illustrates both the analysis and the synthesis tasks. Formula (2.2) readily shows that antenna synthesis $\mathcal{S}$ combines two closely interconnected objectives:

- **Feeding synthesis:** Determine the optimal position, shape, amplitude and phase of the feeder(s) for a fixed antenna geometry Ω to satisfy the performance requirement on metrics $\boldsymbol{p}$.

- **Shape synthesis:** Determine the optimal antenna shape with optimal material distribution for a fixed feeding to satisfy the performance requirement on metrics $\boldsymbol{p}$. This thesis focuses solely on shape synthesis objective, assuming a predetermined shape of the feeding region and its position.
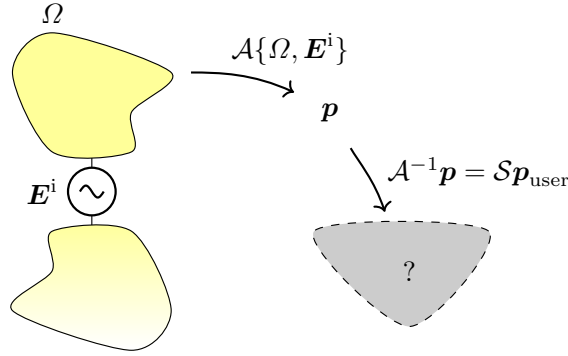
Figure 2.1: Comparison of analysis and synthesis represented as operators $\mathcal{A}$ and $\mathcal{S}$, respectively. Electromagnetic performance p is evaluated for fixed geometry Ω and incident field $\boldsymbol{E}^{\mathrm{i}}$ ($\mathcal{A}$ step). A geometry and feeding should be determined for the user-defined electromagnetic performance p_{user} ($\mathcal{S}$ step).

Formally, shape synthesis task with the assumption of fixed feeding region can be formulated as:

$$
\begin{aligned}
\text{find the structure to satisfy:} \quad & \min \boldsymbol{p} \quad \text{or} \quad p_n < c_n,\ n = \{1, ..., N\}, \\
\text{s.t.} \quad & \text{Maxwell's equations hold,} \quad\quad (2.3) \\
& \text{Design constraints hold,}
\end{aligned}
$$

where $\min \boldsymbol{p}$ is simultaneous minimization of individual metrics. Another approach is a minimization of weighted sum of all metrics [18]. In general, there can be several requirements to the performance metrics $\boldsymbol{p}$, which leads to multi-criteria optimization. Moreover, the constraints dictate the physical validness of the resulting design and compliance with given geometrical restrictions.

Throughout this thesis, Maxwell's equations are represented by electric field integral equation (EFIE) [19]

$$
\boldsymbol{E}^{\mathrm{i}} = \mathcal{L}\left(\boldsymbol{J}\right), \quad\quad\quad (2.4)
$$

where $\boldsymbol{J}$ is an equivalent current density representing the response of the material distribution [20, Chap. 3] and $\boldsymbol{E}^{\mathrm{i}}$ represents the incident electric field. For the problems treated in this thesis, which only contain dielectric materials and perfect electric conductors, we will specifically use electric field integral equation [21], see appendix B for details,

$$\boldsymbol{E}^{\mathrm{i}}\left(\boldsymbol{r}\right) = \rho\left(\boldsymbol{r}\right)\boldsymbol{J}\left(\boldsymbol{r}\right) + \mathrm{j}\omega\mu \int_{\Omega'} \overline{\mathbf{G}}\left(\boldsymbol{r},\boldsymbol{r}'\right) \cdot \boldsymbol{J}\left(\boldsymbol{r}'\right) \, \mathrm{d}\boldsymbol{r}', \tag{2.5}$$

where $\rho\left(\boldsymbol{r}\right)$ is space-dependent complex resistivity, which typically refers to a volumetric current distribution, while for surface distribution is the resistivity substituted by a surface impedance [22]

$$\rho\left(\boldsymbol{r}\right) \to \frac{1}{\mathrm{j}\omega\varepsilon_0\chi\left(\boldsymbol{r}\right)} \quad \text{in Volume EFIE} \tag{2.6}$$

$$\rho\left(\boldsymbol{r}\right) \to Z_s\left(\boldsymbol{r}\right) \quad \text{in Surface EFIE} \tag{2.7}$$

and $\overline{\mathbf{G}}\left(\boldsymbol{r},\boldsymbol{r}'\right)$ is dyadic Green's function [23]

$$\overline{\mathbf{G}}\left(\boldsymbol{r},\boldsymbol{r}'\right) = \left[\mathbb{I} + \frac{1}{k^2}\nabla\nabla\right] \frac{\mathrm{e}^{-\mathrm{j}k|\boldsymbol{r}-\boldsymbol{r}'|}}{4\pi|\boldsymbol{r}-\boldsymbol{r}'|}, \tag{2.8}$$

with $k = \omega\sqrt{\mu\varepsilon}$ denoting wave-number and $\mathbb{I}$ denoting the unit dyad. Furthermore, the arbitrary antenna metric p is evaluated from source current as

$$p = f\left(\boldsymbol{J}\left(\boldsymbol{r}'\right)\right), \quad \boldsymbol{r}' \in \Omega, \tag{2.9}$$

where f denotes arbitrary functional.

In order to solve operator equation (2.4), MoM with basis functions $\{\boldsymbol{\psi}_n(\boldsymbol{r})\}$, see appendix C for details, is used to recast (2.4) into a linear equation system

$$\mathbf{V} = \left(\mathbf{Z}_{\mathrm{G}} + \boldsymbol{\Psi}(\rho)\right)\mathbf{I} = \mathbf{Z}\mathbf{I}, \tag{2.10}$$

where the vector $\mathbf{V} \in \mathbb{C}^{N\times 1}$ represents excitation, $\mathbf{Z}_{\mathrm{G}} \in \mathbb{C}^{N\times N}$ is the impedance matrix characterizing the system, and $\boldsymbol{\Psi}$ is basis function Gram matrix [24]. They are defined element-wise as

$$V_m = \int_{\Omega} \boldsymbol{\psi}_m(\boldsymbol{r}) \cdot \boldsymbol{E}^{\mathrm{i}}\left(\boldsymbol{r}\right) \, \mathrm{d}\boldsymbol{r} \tag{2.11}$$

$$Z_{mn,\mathrm{G}} = \mathrm{j}\omega\mu \int_{\Omega}\int_{\Omega'} \boldsymbol{\psi}_m(\boldsymbol{r}) \cdot \overline{\mathbf{G}}\left(\boldsymbol{r},\boldsymbol{r}'\right) \cdot \boldsymbol{\psi}_n\left(\boldsymbol{r}'\right) \, \mathrm{d}\boldsymbol{r}' \, \mathrm{d}\boldsymbol{r} \tag{2.12}$$

$$\Psi_{mn}(\rho) = \int_{\Omega} \boldsymbol{\psi}_m(\boldsymbol{r}) \cdot \rho(\boldsymbol{r})\boldsymbol{\psi}_n(\boldsymbol{r}) \, \mathrm{d}\boldsymbol{r}. \tag{2.13}$$

Moreover, impedance matrix $\mathbf{Z}$ can be rewritten as

$$\mathbf{Z} = \mathbf{R} + \boldsymbol{\Psi}(\rho) + \mathrm{j}\mathbf{X}, \tag{2.14}$$

where $\mathbf{R}$ is radiation resistance and $\mathbf{X}$ is reactance matrix. System (2.10) allows direct matrix inversion of the impedance matrix to acquire solution.

Consequently, within MoM paradigm, all analytical formulas are expressed in algebraic forms [14], *e.g.*, consider an antenna metric quadratically-dependent on current and physical operator $\mathcal{L}$ which is represented in the basis $\{\boldsymbol{\psi}_n(\boldsymbol{r})\}$ as

$$p \approx \mathbf{I}^{\mathrm{H}}\mathbf{L}\mathbf{I}, \quad \mathbf{L} = [L_{mn}], \quad L_{mn} = \int_{\Omega} \boldsymbol{\psi}_m \cdot \mathcal{L}(\boldsymbol{\psi}_n)\,\mathrm{d}\boldsymbol{r}. \tag{2.15}$$

The synthesis task within MoM paradigm is expressed as a general optimization problem. The geometry of the structure is described by the set of N design variables $\{\boldsymbol{x}_i\}$ and the performance metric p is evaluated from the current vector $\mathbf{I}$. Optimization task reads: find the particular values of design variables (describing shape or topology) that minimize the antenna performance metric p with the fixed feeding vector $\mathbf{V}$ and the set of the inequality and equality design constraints

$$\begin{aligned} \min_{\boldsymbol{x}_i} \quad & p(\boldsymbol{x}_i, \mathbf{I}) \\ \text{s.t.} \quad & c_i(\boldsymbol{x}_i, \mathbf{I}) < 0 \\ & c_j(\boldsymbol{x}_i, \mathbf{I}) = 0 \\ & x_l < x_{ij} < x_u, \ j = \{1, ..., N\} \\ & \mathbf{I}(\boldsymbol{x}_i) = \mathbf{Z}^{-1}(\boldsymbol{x}_i)\mathbf{V}. \end{aligned} \tag{2.16}$$

The set of design constraints is introduced to ensure the physical validity of the optimized problem, such as passivity and limit the optimized region's extent.

Subsequent section 2.1 presents solution methods that can be employed on the optimization task (2.16). Solution methods can be combined with different parametrizations and formulations of the problem, which are described in section 2.2.

■ 2.1 Solution methods

Consider the naive implementation of the synthesis task, *e.g.*, an exhaustive search [25], in which design variables are repetitively varied, and a full-wave electromagnetic simulator evaluates the antenna metric for every parameter step. The computational burden of this approach scales exponentially with the number of design parameters, and it is convenient and inevitable to employ different methods for a large set of parameters in (2.16).

Local techniques often utilize gradient-based algorithms [7], which requires knowledge of the gradients (sensitivities) of antenna metrics $\boldsymbol{p}$ and constraints with respect to designable variables $\boldsymbol{x}_i$. Sensitivities can be approximated using finite differences, which means solving the system equations for each perturbation of the design variable (Topology sensitivity algorithm, section 2.2.4). Another approach is the employment of adjoint sensitivity analysis [11], which only requires solving a single equation for an antenna metric and one for each constraint, and which is independent of the size of

the design domain. Adjoint sensitivity analysis serves as a cornerstone of topology optimization (section 2.2.3). Recently, adjoint sensitivity techniques have been implemented in commercial EM software, *e.g.*, CST Studio Suite [5] with Trust Region Framework or FEKO [4].

General optimization task often consists of countless local minimas resulting in local optimization techniques becoming insufficient. Therefore, global optimization algorithms are employed. Global algorithms, *e.g.*, genetic algorithms [26] or particle swarm optimization [27] algorithms seek inspiration in nature-like mechanisms like gene reproduction, mutation, or recombination. It is anticipated that global optimization techniques can guarantee to reach (near-)optimal design with particular circumstances compared to the local techniques. A prominent class is formed by genetic algorithms (GA) [28], *e.g.*, Non-dominated Sorting Genetic Algorithm II (NSGA-II) [18]. Genetic algorithms are directly compatible with the binary representation of an optimized structure within MoM and have been already employed in electromagnetics [13].

Both techniques, local and global, may be combined into a memetic algorithm (MA) [29]. The local step updates the shape of the structure via gradient algorithm, and GA maintains diversity and resets the local step from being trapped in the local optimum, *i.e.*, GA enlarges the solution space by moving solely through an optimization task's local optima. Generally, MA converges faster due to the local step with less agents than common heuristics [30].

2.2 Problem formulation and design's parametrization

Optimization tasks within different paradigms are formulated and parameterized similarly as in the (2.16) and are presented in subsequent sections. Firstly, the typical parametric model synthesis is introduced in section 2.2.1. The differences between shape and topology optimization and their usage are discussed in section 2.2.2 and section 2.2.3. Finally, section 2.2.4 presents a new optimization paradigm-topology sensitivity algorithm based on exact re-analysis.

2.2.1 Parametric model

The most straightforward approach to antenna design task is a sweep over a set of design parameters. The geometry-related parameters are often considered as designable variables for antenna synthesis.

As an example, consider the N-element Yagi-Uda antenna, see figure 2.2, described by a set of geometrical parameters, *e.g.*, distance D_i between elements and length L_i of each element. The shape of all elements, the building material and the feeding network is fixed. Based on such parametrization,
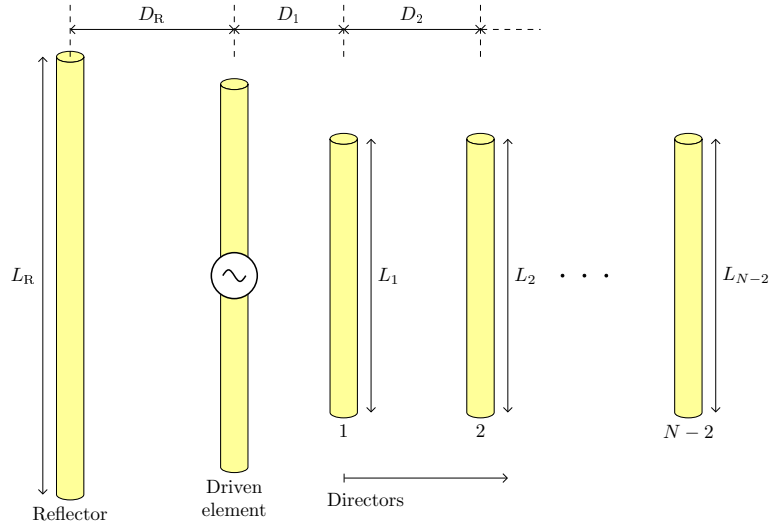
Figure 2.2: Parametric study of N-element Yagi-Uda antenna.

the optimization task (2.16) can be rewritten as

$$\begin{aligned}
\min_{L_i, D_i} \quad & p(L_i, D_i, \mathbf{I}) \\
\text{s.t.} \quad & L_l \leq L_i \leq L_u \\
& D_l \leq D_i \leq D_u \\
& \mathbf{I}(L_i, D_i) = \mathbf{Z}^{-1}(L_i, D_i)\,\mathbf{V} \\
& i = \{1, 2, \ldots, N\}.
\end{aligned} \tag{2.17}$$

Surrogate-based optimization [31] (SBO) can be considered as an advanced type of parametric optimization. The key idea of SBO is that the original electromagnetic problem is represented via computationally cheap representation called a surrogate model [10]. Direct optimization is then replaced by an iterative procedure, where the optimum design is pinpointed by an optimizing of a cheap surrogate model in the previous iteration [32]. It is possible to construct and employ such a model to obtain a satisfactory design with lower computational effort than conventional optimization techniques [10].

■ 2.2.2 Shape optimization

Traditionally, a shape of the structure is defined by a set of boundary curves or surfaces, and in shape optimization, an optimal form of these boundaries is computed. Shape optimization can be considered to be an enhanced parametric model since it can only change the boundary in a sophisticated way, *e.g.*, varying a triangular hole into a rounded one, see figure 2.3. A crucial part is handling boundary perturbation during the optimization process since a reasonably detailed prediction requires a very fine FEM model [33].

Shape optimization methods are used primarily to design elastic structures, *e.g.*, cars [34], acoustic horns [35], but was also employed to optimize
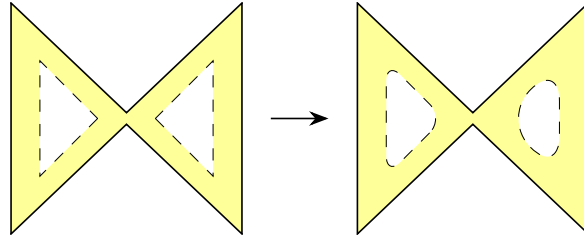
Figure 2.3: Shape optimization.

electromagnetic structures' shapes [36].

2.2.3 Topology optimization

Topology optimization method was primarily developed to design linearly elastic structures [11], [37]. Later on, the method was successfully employed to electromagnetic designs as well, *e.g.*, to structural design in photonics [38], [39], metamaterials [40], electrically small antennas [41], and many others.

Topology optimization of the structure produces non-intuitive designs with geometric features such as connectivity of the structure, the shape of the boundary or number and location of holes [11], resulting in unconventional topologies[2], see figure 2.4. The goal of topology optimization is to determine the optimal layout of a structure within a specified domain. The geometry is not introduced as a set of parameters (as in parametric model representation, see section 2.2.1) but rather by a set of subdomain functions defined over the discretized structure. Therefore, the goal is to find the optimal displacement of given material, *i.e.*, whether each element contains material or not. This problem (0/1) originates from integer programming [25] and is considered to be one of the NP-hard problems [6].
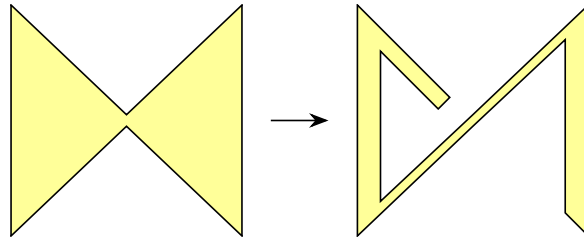
Figure 2.4: Topology optimization.

Topology optimization method commonly replaces the integer variable with a continuous one. This relaxation allows for the employment of mathematical programming methods for continuous problems. Furthermore, it introduces some penalty function that steers the solution to discrete $\{0, 1\}$ values, *e.g.*, by introducing artificial attenuation [39] or/and filtering and thresholding procedure [42]. With this approach, topology optimization can

---

[2]The topology means the connectivity of the structure, which describes both the shape of boundary and holes in it.

alter the structure configuration by creating and disrupting holes, which leads to unconventional designs.

However, using topology optimization within FEM paradigm for designing open boundary problems can lead to the optimization being inefficient since the entire solution domain, including the extra free-space part, is meshed. Recent works therefore also deal with MoM formulation of field integral equations [43], [44], [45], exploiting its advantageous description for planar metallic structures in radiating free space.

Liu *et al.* [43] adopted the adjoint formulation of topology optimization to MoM and demonstrated its feasibility and performance in the design of planar metallic antennas. The optimization task of maximizing the total efficiency at target frequencies is formulated as

$$
\begin{aligned}
\text{find} \quad & \boldsymbol{\rho} \in [0,1]^{1 \times N_e}, \\
\min_{\boldsymbol{\rho}} \quad & -\sum_{k=1}^{N_f} \eta\left(\boldsymbol{\rho}, \mathbf{I}\right)|_{f_k}, \\
\text{s.t.} \quad & \mathbf{I}\left(\boldsymbol{\rho}\right) = \left(\mathbf{Z}_G + \boldsymbol{\Psi}(\boldsymbol{\rho})\right)^{-1} \mathbf{V}, \\
& \sum_{l=1}^{N_e} \rho_l s_l \leq S \sum_{l=1}^{N_e} s_l,
\end{aligned}
\tag{2.18}
$$

where N_e is the total number of elements defining the size of designable variable $\boldsymbol{\rho}$, f_k represents target frequencies, s_l is the area of each element, and S is the ratio of the area occupied by metal to the design domain.

The design domain is a $0.21 \, \text{m} \times 0.20 \, \text{m}$ PEC plate with the total number of 1680 design variables (triangles). Target frequencies are 370 MHz and 420 MHz. The optimal design is obtained after 7.3 min running time[3]. The resulting design contains greyscale elements removed by setting a threshold value for the design variable. Figure 2.5 presents the optimal obtained design by Liu *et al.* [44] in comparison to the classical bow-tie antenna. The bow-tie antenna demands the altering to maximize the total efficiency at target frequencies. The proposed optimization procedure is a good starting point for comparing the developed optimization framework presented in this thesis.

■ 2.2.4 Topology sensitivity algorithm based on exact re-analysis with edge perturbation scheme

The topology sensitivity algorithm [12], [47], developed at the department of the electromagnetic field, is an antenna synthesis method, which can be considered a special case of topology optimization, see section 2.2.3.

The topology sensitivity algorithm works within MoM paradigm, and in its original version, the topology perturbation is performed directly over basis functions rather than over the discretization elements. It is, therefore, the total number of basis functions N that limits the degrees of freedom (DOF) for the algorithm.

---

[3]Four $2.80 \, \text{GHz}$ CPU cores and $4 \, \text{GB}$ RAM.
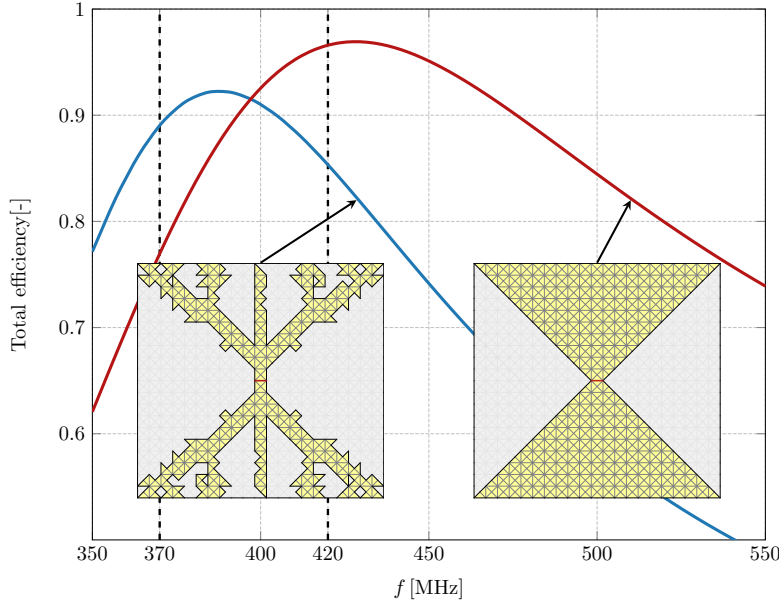
Figure 2.5: The realized total efficiency of two similar planar metallic antennas. The left design (reproduced from [44]) is obtained by the adjoint formulation of TO+MoM based optimization. Designs are analyzed in Antenna Toolbox for MATLAB (AToM) [46].

Most rigorously, the shape synthesis can be defined as an optimization task: For a given impedance matrix $\mathbf{Z}$, matrix $\mathbf{A}$ defining an optimized metric, matrices $\{\mathbf{B}_n\}$ and $\{\mathbf{B}_m\}$ generating constraints, and excitation vector $\mathbf{V}$, find a shape such that

$$
\begin{aligned}
\min_{\mathbf{g}_i} \quad & \mathbf{I}^{\mathrm{H}}\mathbf{A}(\mathbf{g}_i)\mathbf{I} \\
\text{s.t.} \quad & \mathbf{I}^{\mathrm{H}}\mathbf{B}_n(\mathbf{g}_i)\mathbf{I} = b_n \\
& \mathbf{I}^{\mathrm{H}}\mathbf{B}_m(\mathbf{g}_i)\mathbf{I} \leq b_m \\
& \mathbf{I}(\mathbf{g}_i) = \mathbf{Z}^{-1}(\mathbf{g}_i)\mathbf{V}
\end{aligned}
\tag{2.19}
$$

where the third constraint ensures that a solution $\mathbf{g}_i$ solves the MoM equation. Since $\mathbf{g}_i$ is a binary vector, *i.e.*, the problem is of combinatorial nature, and the equality constraints might not be satisfied since there is only a discrete number of solutions. Therefore, the general optimization task (2.19) is relaxed as

$$
\begin{aligned}
\min_{\mathbf{g}_i} \quad & p\left(\mathbf{I}, \mathbf{g}_i\right) \\
\text{s.t.} \quad & \mathbf{I}(\mathbf{g}_i) = \mathbf{Z}^{-1}(\mathbf{g}_i)\mathbf{V} \\
& \mathbf{g}_i \in \{0, 1\}^N,
\end{aligned}
\tag{2.20}
$$

where optimized antenna metric p aggregates constraints from (2.19) and

13

weights them accordingly

$$p\left(\mathbf{I}, \mathbf{g}_i\right) = \mathbf{I}^{\mathrm{H}}\mathbf{A}(\mathbf{g}_i)\mathbf{I}+$$
$$+ \alpha \left|\mathbf{I}^{\mathrm{H}}\mathbf{B}_n(\mathbf{g}_i)\mathbf{I} - b_n\right| + \beta \left|\mathbf{I}^{\mathrm{H}}\mathbf{B}_m(\mathbf{g}_i)\mathbf{I} + u_m - b_m\right|, \qquad (2.21)$$

where inequality constraints are converted into equality constraints by introducing slack variable $u_m \geq 0$ for each of them [8]. Generally, antenna metric p can be composed as a combination of several physical and geometrical metrics.

As opposed to the topology optimization, see section 2.2.3, the algorithm does not introduce a continuous variable for each element but tries to directly solve an integer programming task (2.20) by introducing an inversion-free rank-1 modification of the impedance matrix, *i.e.*, basis function removal or addition, based on exact re-analysis [48]. The fundamental approach to inversion-free modification is the utilization of Sherman-Morrison-Woodbury(SMW) identity [49], which significantly reduces computational burden [47] as opposed to classical pixeling technique [13]. The topology sensitivity algorithm is implemented as a package in an in-house built EM simulator AToM [46].

In order to demonstrate working principle of topology sensitivity algorithm based on exact re-analysis, consider a synthesis problem of minimizing the radiation Q-factor [24] of an electrically small antenna ($ka < 1$). Q-factor inversely proportional to fractional bandwidth (FBW) [50] is defined on the condition that the antenna is in resonance. Therefore, we assume connection of an ideal tuning[4]. The Q-factor minimization task is prescribed as

$$\begin{aligned} \min_{\mathbf{g}_i} \quad & Q\left(\mathbf{I}\right) \\ \text{s.t.} \quad & \mathbf{I}(\mathbf{g}_i) = \mathbf{Z}(\mathbf{g}_i)^{-1}\mathbf{V}, \qquad (2.22) \\ & \mathbf{g}_i \in \{0,1\}^N, \end{aligned}$$

where Q-factor is defined as

$$Q\left(\mathbf{I}\right) = \frac{2\omega \max\{W_{\mathrm{m}}(\mathbf{I}), W_{\mathrm{e}}(\mathbf{I})\}}{P_{\mathrm{rad}}(\mathbf{I})}, \qquad (2.23)$$

where P_{rad} is radiated power and W_{e} and W_{m} represent stored electric and magnetic energy [51], respectively. Figure 2.6 presents optimal topology of plate made of perfect electric conductor (PEC) found via the topology sensitivity algorithm minimizing the radiating Q-factor for $ka < 0.5$.

Although the designs generated with topology sensitivity algorithm outperforms empirically found designs, the crucial problem is the interpretation of the basis function removal.

The problem is that a single basis function removal does not have a simple interpretation of the physical modification of a structure. However, it can be represented as a cut-out slot alongside the edge corresponding to the removed basis function [47], see figure 2.7. The essential question

---

[4]Self-resonance can also be acquired via suitable shape design.
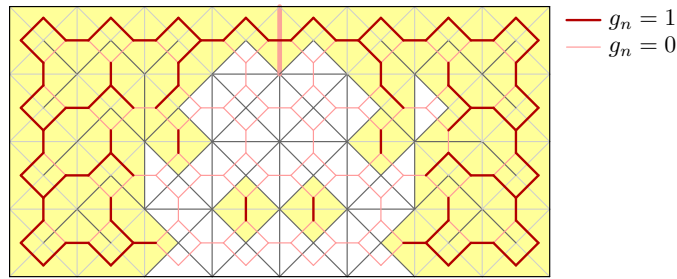
Figure 2.6: Optimal topology of a PEC plate with $ka = 0.5$, reaching minimal quality factor $Q/Q_{\mathrm{lb}} = 1.4$. Enabled and disabled basis functions are depicted by a red thick and thin line, respectively. Delta gap excitation [52] is horizontally centred in the upper row and is highlighted by the pink transparent color.

regards the thickness of a slot since an edge is considered to be infinitesimally small. Consequently, the final optimized structure is not likely to be easily manufactured and requires additional regularization constraints.

$$\text{Edge removal} \rightarrow \boxed{d_{\mathrm{slot}}} = ?$$
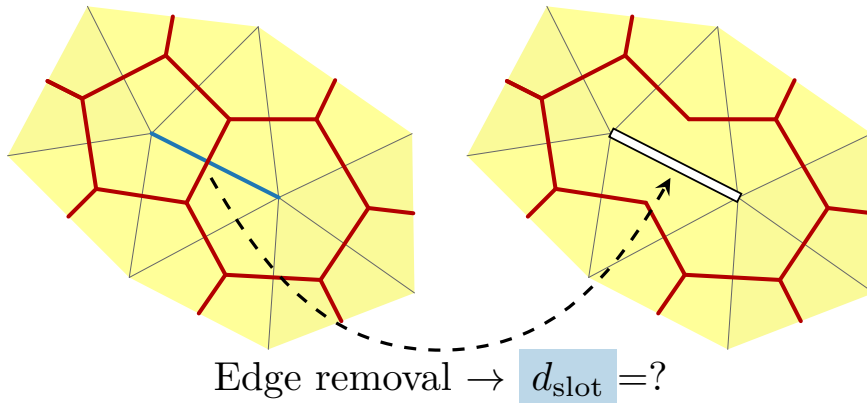
Figure 2.7: Removal of an edge does not have simple geometrical interpretation. How wide slot should be carved out?

Chapter 3

Topology sensitivity algorithm based on exact re-analysis

Optimization of electromagnetic structures with the topology sensitivity algorithm is based on the differences induced by the smallest perturbations of the structure. In principle, the addition or removal of a basis function can be considered the smallest modification of a structure. This choice, however, exhibits interpretation issues, see section 2.2.4. The topology sensitivity algorithm based on exact re-analysis [12], [48] with an addition or removal of one mesh element is therefore developed in this chapter.

Let us consider an electromagnetic structure analyzed by MoM. In order to solve the electromagnetic problem described by a linear system (2.10), with impedance matrix $\mathbf{Z}$ (analysis step) and excitation vector $\mathbf{V}$, the matrix inversion is required

$$\mathbf{I} = \mathbf{Z}^{-1}\mathbf{V} = \mathbf{Y}\mathbf{V}, \tag{3.1}$$

with $\mathbf{Y}$ being the admittance matrix. As a particular example, but without lost of generality, the subsequent sections assume a utilization of surface electric field integral equation (SMoM) with Rao-Wilton-Glisson (RWG) basis functions [53] and of volumetric electric field integral equation (VMoM) with piece-wise constant basis functions [54], which are available in electromagnetic simulator AToM [55] developed at the department of electromagnetic field. For more details about the aforementioned basis functions see appendix C.1.

The properties of the developed algorithm are dependent on the particular basis functions used, and, therefore, an implementation significantly differs between the SMoM and VMoM. Nevertheless, the mathematical background for the developed algorithm is identical as they share the description via (3.1).

Initial structures are discretized, see figure 3.1, delimiting the bounding box, *i.e.*, the maximal region spanned by the optimized structure $\Omega_i \subseteq \Omega_0$. A discretization is fixed during the optimization procedure, limiting achievable details in the structure, nevertheless accelerating the optimization's search for a solution since the MoM matrices are evaluated only once at the beginning of the procedure.

Consider further a discretized structure Ω_0 that is represented with N basis functions. The solution space of a binary optimization over basis functions has dimension 2^N, while binary optimization over mesh elements
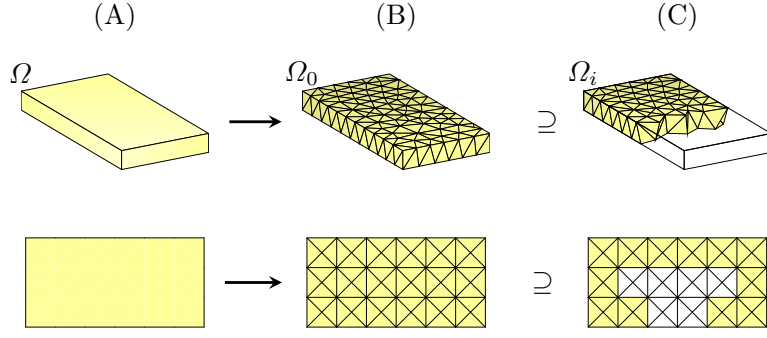
Figure 3.1: (A) Continuous structure Ω is discretized into a set of tetrahedrons (slab) or triangles (plate). (B) Discretized structure Ω_0 delimits the maximal region spanned by the particular shape (C), *i.e.*, $\Omega_i \subseteq \Omega_0$.

operates with solution space of dimensions 2^T, with $T < N$, see table 3.1. Moreover, the employment of piece-wise constant basis functions leads to an apparent reduction of the solution space due to the exact relation between the number of tetrahedrons and basis functions, *i.e.*, $T = 3N$. The optimization over mesh elements thus reduces computational time, removes interpretations difficulties but, on the other hand, sacrifices resolution[1].
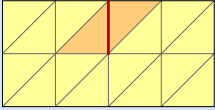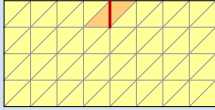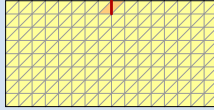
N edges	18	84	360
Solutions	$1.3 \cdot 10^5$	$9.7 \cdot 10^{24}$	$1.2 \cdot 10^{108}$
T triangles	16	64	256
Solutions	$1.6 \cdot 10^4$	$4.6 \cdot 10^{18}$	$2.9 \cdot 10^{76}$

Table 3.1: The complexity of structural optimization for the given number of unknowns N and corresponding number of triangles T. The red vertical line represents localized (delta gap) feeding, *i.e.*, two neighbouring triangles must be fixed during the optimization process.

In this thesis, we solely focus on binary optimization, *i.e.*, presence or absence of a mesh element $\{0, 1\}$. However, arbitrary material (represented by resistivity ρ) can be assigned to a discretization element $\{\rho_1, \rho_2, \ldots, \rho_S\}$ modifying the binary optimization to general multi-state integer optimization, effectively obtaining larger solution space, *i.e.*, S^T with S being the number of states. Multi-state topology sensitivity is out of the scope of this thesis.

---

[1]Manipulation with mesh elements often requires modification of more than one basis function.

■ 3.1 Computational complexity of a naive synthesis algorithm within MoM

Let us investigate the computational complexity of the naive approach to the synthesis, *i.e.*, iterative evaluation of an antenna metric after a small structural modification, see figure 3.2. The impedance matrix is inverted (3.1) each time the structure is altered by standard LU-decomposition algorithm [56] with the computational complexity of $\mathcal{O}(N^3)$.

It is proven, that matrix inversion is equivalent to matrix multiplication [6], *i.e.*, if $t(N)$ denotes the time of multiplication of two $N \times N$ matrices, then the time to invert an $N \times N$ matrix is of the order $\mathcal{O}(t(N))$. Table 3.2 summarizes matrix multiplication algorithms and their computational complexities. Nevertheless, the best complexity is determined under the assumption of sufficiently large matrices, *i.e.*, so enormous that the algorithm is never used in practice, *i.e.*, making it a galactic algorithm [57]. Consequently, Strassen's multiplication algorithm is often combined with standard inversion algorithms to enhance their computational complexity. Without loss of generality, we will assume standard LU-decomposition with $\mathcal{O}(N^3)$.
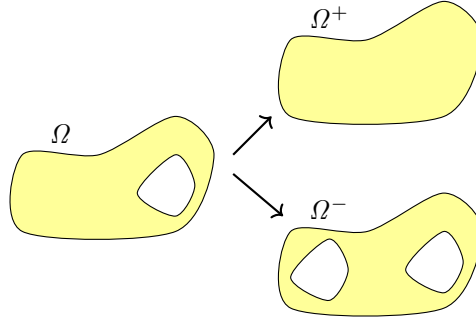
Figure 3.2: Possible structural modification of the initial topology of a structure Ω.

Computational complexity is increased to $\mathcal{O}(N^3 M)$ with M being a set of elements to be removed or added. This computation has to be repeated in I iterations while modifying a structure. Thus, the optimization by an exhaustive search is proportional to $\mathcal{O}(N^3 M I)$.

Matrix multiplication algorithm	Year	Computational complexity
Naive algorithm	1950	$\mathcal{O}(N^3)$
Strassen's algorithm [58]	1969	$\mathcal{O}(N^{2.807})$
Coppersmith-Winograd algorithm [59]	1990	$\mathcal{O}(N^{2.376})$

Table 3.2: Computational complexity of matrix multiplication algorithms throughout the past decades.

Typically, M equals N(or they are at least proportional) since we perform as many removals/additions as the number of DOFs. Similar consideration

19

is valid for I, reaching an algorithm with computational complexity $\mathcal{O}(N^5)$, which is a considerable computational burden. The inversion of a matrix (with $\mathcal{O}(N^3)$) is the most considerable burden. For this reason, the inversion-free formulas [49], see appendix D for details, shall be used to accelerate the optimization process.

◼ 3.2 Structure representation

Before the take advantage of inversion-free formulas, the mesh grid must be properly parametrized. Within the used description, the unknown current $\mathbf{I}$ is evaluated as

$$\mathbf{I}(\mathbf{g}_i) = \mathbf{Z}^{-1}(\mathbf{g}_i)\mathbf{V}, \tag{3.2}$$

where the binary vector $\mathbf{g}_i \in \{0,1\}^{N \times 1}$ of disabled/enabled basis functions represents the i-th modifcation of an initial shape. In order to parametrize the structure directly by a logical vector of disabled/enabled mesh elements, the incidence matrix [60], mapping the basis functions to the underlying discretization elements, is employed. The procedure is first presented on a planar structure with RWG, *i.e.*, overlapping, basis functions [53], [61]. Afterwards, the parametrization of volumetric tetrahedral mesh with piecewise constant basis functions is developed.

Assume a planar metallic structures discretized into a set of triangular patches analyzed by SMoM with RWG basis functions. All shapes derived from the initial shape Ω_0 can be also represented by the binary vector $\mathbf{t}_i \in \{0,1\}^{T \times 1}$ of disabled/enabled triangles, which is related to $\mathbf{g}_i$ as

$$\mathbf{t}_i = \mathcal{B}\left(\mathbf{Mg}_i\right), \tag{3.3}$$

where $\mathbf{M} \in \{0,1\}^{T \times N}$ is the incidence matrix [62] and $\mathcal{B}(.)$ represents the Boolean operator, which substitutes all non-zero entries of the matrix to one and all negative entries to zero. Figure 3.3 presents a particular example of such parametrization.

The vector $\mathbf{t}_i$ should be subjected to binary optimization, but it is the vector $\mathbf{g}_i$ that enters the matrix description (3.2). However, the opposite relation to (3.3) is non-unique, *i.e.*, same metallization $\mathbf{t}_i$ can be formed via different vectors $\mathbf{g}_i$. Therefore, let us investigate an opposite relation. Each row of transposed incidence matrix $\mathbf{M}^\mathrm{T}$ contains two non-zero entries, *i.e.*, two adjacent triangles sharing an edge. Therefore, a product of multiplication $\mathbf{M}^\mathrm{T}\mathbf{t}_i$ contains unwanted zeros or ones[2] and wanted twos[3]. Thus, the relation is defined via additional operations to obtain logical vector $\mathbf{g}_i$ as

$$\mathbf{g}_i = \neg\mathcal{B}\left(\mathbf{M}^\mathrm{T}\mathbf{t}_i - 2\right), \tag{3.4}$$

where $\neg$ denotes logical negation [63]. Formula (3.4) is valid relation for the purposes of this thesis, where a basis function shared by two mesh elements is always enabled.

---

[2]None or one of these two triangles is enabled.

[3]Both of these triangles are enabled.
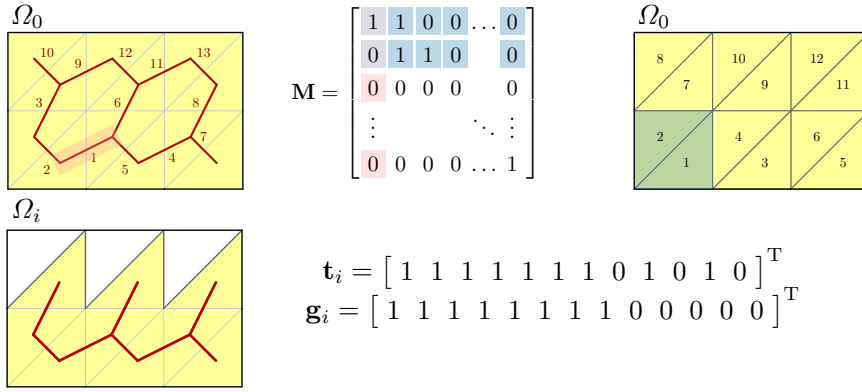
Figure 3.3: The initial shape Ω_0 is discretized into $T = 12$ triangles and $N = 13$ overlapping basis functions (numbered red lines). The incidence matrix $\mathbf{M}$ maps basis functions onto triangles and vice versa. Highlighted rows (columns) represent particular triangles (basis functions). A particular shape $\Omega_i \subseteq \Omega_0$ can be represented by the binary vector $\mathbf{t}_i$ or $\mathbf{g}_i$. The enabled triangles and basis functions are highlighted by yellow and red color, respectively.

As an alternative to the surface MoM, let us assume a volumetric dielectric body discretized into a set of tetrahedra and piece-wise constant basis functions[4]. The parametrization of volumetric shapes within VMoM is similar to the planar ones. With properly defined incidence matrix $\mathbf{M}$ the relation (3.3) stands. Let us investigate $\mathbf{M}^{\mathrm{T}}$ for non-overlapping basis functions, see appendix C.1. Each row of transposed incidence matrix $\mathbf{M}^{\mathrm{T}}$ with non-overlapping basis functions contains exactly one non-zero entry, *i.e.*, a basis function is not shared between mesh elements. Therefore, the mapping $\mathbf{t}_i \rightarrow \mathbf{g}_i$ is readily given by

$$\mathbf{g}_i = \mathbf{M}^{\mathrm{T}}\mathbf{t}_i. \tag{3.5}$$

Figure 3.4 presents a particular example of such parametrization.

3.3 Mesh element removal

In this section, we introduce a suitable definition of mesh element removal via properly defined logical vectors.

Consider a particular planar shape Ω_i, modelled with SMoM and RWG basis functions, with logical vector $\mathbf{t}_i$ and incidence matrix $\mathbf{M}$. The position and shape of a feed are assumed to be fixed and described by a logical vector $\mathbf{t}_i^{\mathrm{p}}$ of protected triangles, *i.e.*, those not entering the optimization. The set of triangles tested for removal is defined by logical vector $\mathbf{t}_i^{-}$

$$\mathbf{t}_i^{-} = \mathbf{t}_i \oplus \mathbf{t}_i^{\mathrm{p}}, \tag{3.6}$$

where $\oplus$ denotes exclusive disjunction [63] (logical XOR function). The incidence matrix $\mathbf{M}$ contains a piece of information about the connection

---

[4]If Schaubert-Wilton-Glisson (SWG) [64] basis functions will be used, then the VMoM case and SMoM case would be the same.
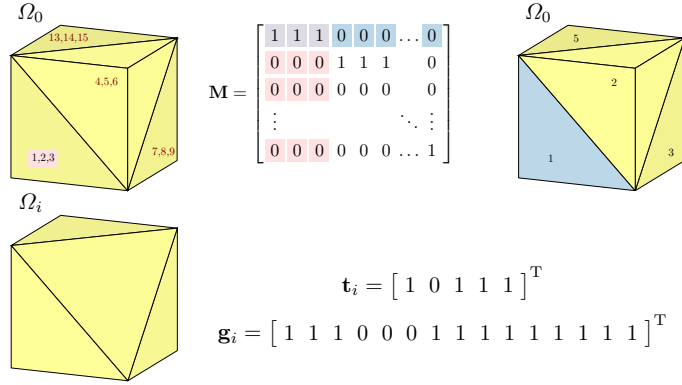
Figure 3.4: The initial shape Ω_0 is discretized into $T = 5$ tetrahedra and $N = 15$ non-overlapping basis functions. The incidence matrix $\mathbf{M}$ maps basis functions onto tetrahedra and vice versa. The highlighted rows (columns) represent particular tetrahedron (basis functions). A particular shape $\Omega_i \subseteq \Omega_0$ can be represented by the binary vector $\mathbf{t}_i$ or $\mathbf{g}_i$. The enabled tetrahedrons and basis functions are not highlighted, since a shape modification is clear.

of each triangle with corresponding basis functions. Therefore, we define a matrix $\mathbf{M}^-$ via Hadamard (element-wise) multiplication[5] $\odot$ [56] as

$$\mathbf{m}_j^- = \left(\mathbf{m}_j \odot \mathbf{g}_i^{\mathrm{T}}\right) t_{ij}^-, \quad j \in \{1, \dots, T\}, \tag{3.7}$$

where $\mathbf{a}_j$ is j-th row of matrix $\mathbf{A}$ and t_{ij}^- is j-th position in the binary vector $\mathbf{t}_i$, *i.e.*, it is an identifier denoting if the j-th mesh element shall be further tested for removal. Each row in $\mathbf{M}^-$ represents the j-th triangle composed of corresponding basis functions. The utilization of overlapping basis functions brings a significant problem in terms of shape resolution while removing elements. Consider a removal situation in figure 3.5, where the red triangle is removed. The red triangle is composed of two basis functions, which are removed. However, a neighboring triangle in the right bottom corner is composed of only one basis function, which is shared with the red triangle. Therefore, the removal of red triangle will cause the removal of another one.

Similarly, we define a set of triangles to be tested for addition. We assume that protected triangles cannot be removed. Therefore, logical vector $\mathbf{t}_i^+$ of tested triangles is

$$\mathbf{t}_i^+ = \neg \mathbf{t}_i. \tag{3.8}$$

Once again, the employment of overlapping basis functions introduces a significant problem in terms of shape resolution while adding elements. Consider a situation in figure 3.5, where the blue triangle composed of two basis functions is added. Since these two basis functions are shared with other triangles, they are also added back to the set of enabled triangles. In order to sustain as high resolution as possible (addition/removal of exactly one triangle), we

---

[5]More exactly element-wise logical conjuction [63] (logical AND function) in the context of binary vectors and matrices.
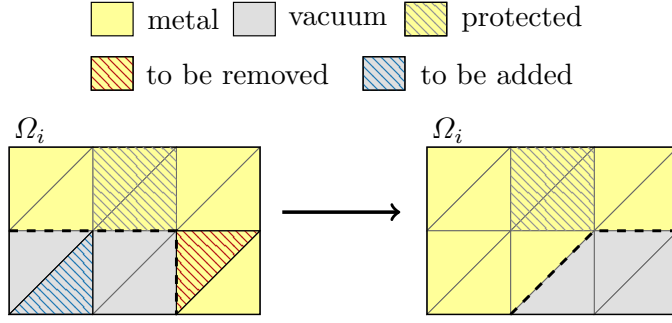
Figure 3.5: Triangle removal/addition issue caused by the employment of overlapping basis functions. A triangle removal/addition can cause the removal/addition of a different triangle since basis functions are shared by two adjacent triangles. The thick dashed line represents an inner shape boundary.

introduce a restriction on the tested set for addition. Notice, in figure 3.5, the inner shape boundary highlighted by the thick dashed line. It is bounded via the shared edge of an enabled and a disabled triangle. Therefore, if we add (enable) this neighboring triangle, we physically add only one triangle. Thus, the addition of a boundary triangle sustains high resolution. Therefore, only boundary triangles are tested for addition, effectively turning the addition process into shape optimization, see section 2.2.2. Nevertheless, the combination of mesh element removal and addition provides sufficiently good structure modification, and any shape is reachable. Consequently, we define the j-th row of matrix $\mathbf{M}^+$ similar to (3.7) as

$$\mathbf{m}_j^+ = \left(\neg \mathbf{g}_i^{\mathrm{T}} \odot \mathbf{m}_j \right) t_{ij}^+, \quad j \in \{1, \dots, T\}, \tag{3.9}$$

where the j-th row represents addition of the j-th mesh element composed of corresponding basis functions. Formula (3.9) is an analogy to the removal case (3.7), however, resulting list $\mathbf{M}^+$ still requires processing of additional restrictions in order to test only triangles next to the shape's boundary for addition.

Similar sets for removals/additions are defined within VMoM with tetrahedral discretization and piece-wise constant basis functions. However, the employed basis functions are non-overlapping, and the issue with multiple removals/additions vanishes. Therefore, non-overlapping basis functions sustain high shape resolution, do not require additional treatment and formulas (3.7) and (3.9) are the same.

3.4 Mesh element removal interpretation

As opposed to classical pixeling technique [65], where the corresponding columns and rows of impedance matrix are removed, we interpret removal in a different manner. Rather than reducing the size of the impedance matrix, we retain it (no mesh element is removed), but we alter the complex

resistance $\rho(\boldsymbol{r})$ of the underlying mesh elements to

$$\rho(\boldsymbol{r}) = R_\infty \qquad \Longleftrightarrow \quad \boldsymbol{r} \in \text{mesh element}, \qquad (3.10)$$

which is arranged by placing an infinity (or a large number) on corresponding diagonal elements of impedance matrix $\mathbf{Z}$ according to figure 3.6. Following matrix inversion zeroes corresponding rows and columns of admittance matrix $\mathbf{Y}$ (consequently, zero current is associated with the removed basis functions). Therefore, columns and rows of $\mathbf{Y}$ containing only zeroes can be removed
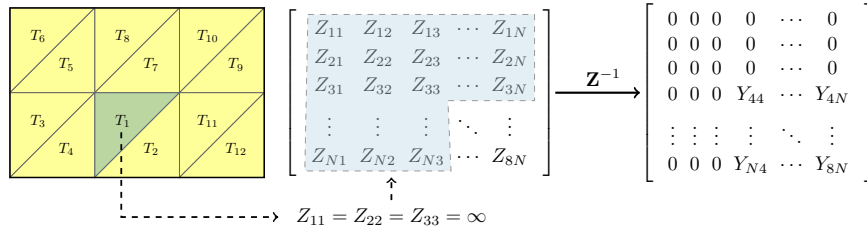
Figure 3.6: Illustration of a triangle removal. The triangular element T_1 is removed via the removal of associated basis functions. This is reflected in the impedance matrix $\mathbf{Z}$ as the infinity placement on the corresponding diagonal element and in the admittance matrix $\mathbf{Y}$ in which corresponding rows and columns are zeroed.

Projection matrix $\mathbf{C}$, which is used to address the corresponding column or row of impedance matrix, is further developed. Each row of matrices $\mathbf{M}^\pm$, introduced in section 3.3, represents a mesh element whose resistance is altered according to (3.10), *i.e.*, it contains a few[6] basis functions which are modified accordingly. The construction of the projection matrix $\mathbf{C}$ is depicted in figure 3.7. Particular mesh element made of a few basis functions corresponds to the row of matrix $\mathbf{M}^-$ which directly provides logical vector $\mathbf{g}$ of these basis functions. Consequently, the projection matrix is defined as

$$\mathbf{C} = \text{diag}\left(\mathbf{g}\right), \qquad (3.11)$$

where $\text{diag}(\mathbf{x})$ is a matrix with vector $\mathbf{x}$ placed on its diagonal, and where all columns of $\mathbf{C}$ containing solely zeros are removed afterwards. Consider an example of multiplication $\mathbf{AC}$ in which the projection matrix picks out corresponding columns.

---

[6]Up to three for overlapping basis functions, exactly three for non-overlapping ones.

$$\mathbf{M}^- = \begin{bmatrix} 1 & 1 & 0 & 1 & \dots & 0 \\ 0 & 1 & 1 & 0 & \dots & 0 \\ 0 & 0 & 0 & 1 & \dots & 0 \\ \vdots & \vdots & \vdots & \vdots & \ddots & \vdots \\ 0 & 0 & 0 & 0 & \dots & 1 \end{bmatrix} \rightarrow \mathbf{g}_1 = \begin{bmatrix} 1 & 1 & 0 & 1 & 0 & \cdots & 0 \end{bmatrix}^{\mathrm{T}}$$

$$\mathbf{C}_1 = \begin{bmatrix} 1 & 0 & 0 \\ 0 & 1 & 0 \\ 0 & 0 & 0 \\ 0 & 0 & 1 \\ \vdots & \vdots & \vdots \\ 0 & 0 & 0 \end{bmatrix} \qquad \begin{bmatrix} A_{11} & A_{12} & A_{13} & A_{14} & \dots & A_{1N} \\ A_{21} & A_{22} & A_{23} & A_{24} & \dots & A_{2N} \\ A_{31} & A_{32} & A_{33} & A_{34} & \dots & A_{3N} \\ A_{41} & A_{42} & A_{43} & A_{44} & \dots & A_{4N} \\ \vdots & \vdots & \vdots & \vdots & \ddots & \vdots \\ A_{N1} & A_{N2} & A_{N3} & A_{N4} & \dots & A_{NN} \end{bmatrix}$$

$$\mathbf{AC}$$

Figure 3.7: Projection matrix **C** for a particular mesh element is constructed from a logical vector **g** of corresponding basis functions and is used to pick out corresponding columns by performing the right matrix multiplication.

Using (3.10) in (3.1) with projection matrix **C** substituted leads to

$$\mathbf{Y} = (\mathbf{Z} + \mathbf{C}R_\infty\mathbf{C}^{\mathrm{T}})^{-1}, \tag{3.12}$$

which after limiting procedure $R_\infty \to \infty$ leads a "removal" of mesh element as its material properties are those of vacuum. Direct inversion (3.12) with infinity on the matrix's diagonal is not possible and requires an analytical approach.

In section 3.5 it is shown that inversion of the impedance matrix **Z** with complex resistivity (3.10) can be formally performed via the Sherman-Morrison-Woodbury (SMW) formula [49], greatly reducing the computational cost.

3.5 Effective structure perturbation

The effective way to avoid repetitive impedance matrix inversion (3.1) with complex resistivity (3.10) is presented in this section. The admittance matrix for particular topology perturbation is derived using inversion-free formulas, see appendix D.

Assume an arbitrary structure (planar metallic/volumetric dielectric) described by the full impedance matrix $\mathbf{Z}_{\mathrm{G}}$ (analysis) and further on consider a particular shape represented by a logical vector $\mathbf{t}_i$, which is related to a logical vector $\mathbf{g}_i$ via the incidence matrix **M**. The matrices $\mathbf{M}^\pm$ are determined according to the section 3.3.

Without loss of generality, assume a general shape with the impedance matrix **Z** provided by $\mathbf{g}_i(\mathbf{t}_i)$, according to figure 3.6. Consequent structural modification of a shape, *i.e.*, mesh element removal, corresponds to

$$\hat{\mathbf{Y}} = \hat{\mathbf{Z}}^{-1} = \left(\mathbf{Z} + \mathbf{C}R_\infty\mathbf{C}^{\mathrm{T}}\right)^{-1}, \tag{3.13}$$

where ˆ represents the perturbated matrix of the investigated shape. In order to evaluate all perturbation of the structure, (3.13) must be performed iteratively, which is computationally demanding. In the following derivation, the modification of the admittance matrix is determined only for one mesh

element, and subsequent section 4.1 presents the vectorization, where all possible modification of an actual shape is evaluated at once.

In order to completely avoid inversion (3.13), we perform SMW formula, see (D.4), on (3.13), which leads to

$$
\left(\mathbf{Z} + \mathbf{C}R_\infty\mathbf{C}^{\mathrm{T}}\right)^{-1} = \mathbf{Y} - \mathbf{Y}\mathbf{C}\left(\frac{\mathbb{I}}{R_\infty} + \mathbf{C}^{\mathrm{T}}\mathbf{Y}\mathbf{C}\right)^{-1}\mathbf{C}^{\mathrm{T}}\mathbf{Y} =
$$
$$
= \mathbf{Y} - \mathbf{Y}\mathbf{C}\left(\mathbf{C}^{\mathrm{T}}\mathbf{Y}\mathbf{C}\right)^{-1}\mathbf{C}^{\mathrm{T}}\mathbf{Y}, \tag{3.14}
$$

where $\mathbb{I}$ is unit matrix sized according to the size of perturbation, *i.e.*, number of basis function to be removed, and where we implicitly used limit $R_\infty \to \infty$. Formula (3.14) still requires matrix inversion, but the admittance matrix $\mathbf{Y}$ is computed only once at the start of the optimization process and, then, all possible modifications are computed by taking inversion of small matrix $\mathbf{C}^{\mathrm{T}}\mathbf{Y}\mathbf{C}$ (3×3 matrix if three basis functions are removed). Formula (3.14) readily shows that removing an element composed of a set of basis functions results in the admittance matrix in which rows and columns corresponding to the basis functions are zeroed.

A sole removal technique is not sufficient for topology modifications, since the non-existence of an element addition may cause a premature deadlock [47]. Thus, the optimization process is extended by the addition of a mesh element. For further clarification assume real indices

$$
\{e\} : \quad \Longleftarrow \quad \mathbf{g}_i \leftarrow \mathbf{t}_i, \tag{3.15}
$$
$$
\{b\} : \quad \Longleftarrow \quad \mathbf{g}_m \leftarrow \mathbf{t}_i^+, \tag{3.16}
$$

which represents enabled edges $\{e\}$ and edges to be added $\{b\}$ (corresponding to a mesh element), respectively. Sets are determined via relation $\leftarrow$ between logical vectors $\mathbf{t}_i$ and $\mathbf{g}_i$ based on employed basis functions. Consequently, a mesh element addition corresponds to the block matrix inversion as

$$
\hat{\mathbf{Y}} = \hat{\mathbf{Z}}^{-1} = \begin{pmatrix} \mathbf{Z}_{\mathrm{G},ee} & \mathbf{Z}_{\mathrm{G},be} \\ \mathbf{Z}_{\mathrm{G},eb} & \mathbf{Z}_{\mathrm{G},bb} \end{pmatrix}^{-1}, \tag{3.17}
$$

where $\mathbf{Z}_{\mathrm{G}}$ is the impedance matrix of a full structure. Performing the block matrix inversion leads to

$$
\hat{\mathbf{Y}} = \begin{pmatrix} \mathbf{Y}_{\mathrm{G},ee} + \mathbf{x}_{eb}\mathbf{y}_{bb}\mathbf{x}_{be}^{\mathrm{T}} & -\mathbf{x}_{eb}\mathbf{y}_{bb} \\ -\mathbf{y}_{bb}\mathbf{x}_{be}^{\mathrm{T}} & -\mathbf{y}_{bb} \end{pmatrix}, \tag{3.18}
$$

with auxiliary variables defined as

$$
\mathbf{x}_{eb} = \mathbf{Y}_{\mathrm{G},ee}\mathbf{Z}_{\mathrm{G},eb},
$$
$$
\mathbf{y}_{bb} = (\mathbf{Z}_{\mathrm{G},bb} - \mathbf{Z}_{\mathrm{G},be}\mathbf{x}_{eb})^{-1}. \tag{3.19}
$$

The Block matrix inversion formula above assumes that a set of basis functions corresponding to the mesh element to be added occupies the last columns and rows of the matrix. Consequently, the admittance matrix $\hat{\mathbf{Y}}$ requires

a sorting mechanism, which provides a correct ordering of basis functions concerning the original impedance matrix of the whole structure Ω_0. For the sake of clarity, we emphasize that updating the admittance matrix in (3.14) and (3.18), *i.e.*, modifying the shape, results in $\hat{\mathbf{Y}}$ turning into $\mathbf{Y}$ in the next iteration since the updated shape is investigated for the structural modification again.

Assuming predefined excitation vector $\mathbf{V}$, admittance matrix modification formulas (3.14) and (3.18) readily provides information about the current perturbation as

$$\text{Removal}: \quad \hat{\mathbf{I}} = \mathbf{I} - \mathbf{YC}\left(\mathbf{C}^{\mathrm{T}}\mathbf{YC}\right)^{-1}\mathbf{C}^{\mathrm{T}}\mathbf{I}, \tag{3.20}$$

$$\text{Addition}: \quad \hat{\mathbf{I}} = \begin{pmatrix} \mathbf{I} \\ \mathbf{0} \end{pmatrix} + \begin{pmatrix} \mathbf{x}_{eb}\mathbf{y}_{bb}\left(\mathbf{Z}_{\mathrm{G},be}\mathbf{I} - \mathbf{V}_b\right) \\ -\mathbf{y}_{bb}\left(\mathbf{Z}_{\mathrm{G},be}\mathbf{I} + \mathbf{V}_b\right) \end{pmatrix}, \tag{3.21}$$

where $\mathbf{I}$ is current impressed by the excitation $\mathbf{V}$ onto a current shape which should be modified.

Current modification formulas (3.20) and (3.21) allow direct accumulation of currents corresponding to all structural perturbations into a matrix

$$[\hat{\mathbf{I}}] = [\hat{\mathbf{Y}}\mathbf{V}] = [\mathbf{I}_{\mathbf{t}_1} \quad \cdots \quad \mathbf{I}_m \quad \cdots \quad \mathbf{I}_{\mathbf{t}_T}], \quad m \Longleftarrow \mathbf{t}_i^{\pm}, \tag{3.22}$$

where every tested mesh element is determined by procedures defined earlier and where a column represents the current after element removal/addition.

▌ 3.6   Topology sensitivity

Qualitative description of how effective is a perturbation in terms of antenna performance p needs to be evaluated for each perturbation column of current matrix (3.22). The topology sensitivity $\tau(p)$ is defined here as

$$\tau(p, \mathbf{t}_i) = p([\hat{\mathbf{I}}]) - p(\mathbf{I}) \approx \nabla p(\mathbf{I}). \tag{3.23}$$

A shape is modified as long as a mesh element with a negative value of topology sensitivity $\tau(p)$ exists, *i.e.*, as long as there is a possibility of improving the performance. When all the sensitivities are non-negative, the shape is said to be locally optimal.

▌ 3.7   Optimization task

Optimization task within defined formalism is considered to be a binary problem: for a structure with the impedance matrix $\mathbf{Z}$, find its shape, *i.e.*, logical vector $\mathbf{t}_i$ of disabled/enabled triangles, so that

$$\begin{aligned} \min_{\mathbf{t}_i} \quad & p\left(\mathbf{I}, \mathbf{g}_i\right) \\ \text{s.t.} \quad & \mathbf{I}(\mathbf{g}_i) = \mathbf{Z}^{-1}(\mathbf{g}_i)\mathbf{V} \\ & \mathbf{g}_i = f\left(\mathbf{t}_i\right) \\ & \mathbf{t}_i \in \{0,1\}^T, \end{aligned} \tag{3.24}$$

where p is an optimized metric and f denotes proper relation between both logical vectors, *i.e.*, formula (3.4) and (3.5) for overlapping and non-overlapping basis functions, respectively. The first governing equation secures that the equation (3.1) is satisfied. The second governing equation relates to the geometry and gives a map between logical vectors $\mathbf{t}_i$ and $\mathbf{g}_i$, since optimization unknowns are the mesh pixels, but electromagnetic quantities are evaluated over the basis functions.

Antenna metric p can aggregate arbitrary combination of physical p_1 and geometrical metrics q

$$p(\mathbf{I}, \mathbf{g}_i) = p_1(\mathbf{I}) + \alpha q(\mathbf{g}_i, \mathbf{t}_i), \tag{3.25}$$

which readily provides suitable partition of physical and geometrical requirements. Geometrical requirements are crucial in terms of shape's regularity, *i.e.*, according to manufacturing demands. Two geometrical metrics are introduced in the next section to ensure manufacturing feasibility of designs.

◾ 3.8 Geometrical metrics

Geometrical metrics are introduced in order to ease the manufacturing process. These metrics are employed only on planar structure analyzed by SMoM, but can also be generalized to the volumetric case.

Isolated islands of material are generally unwanted products of topology optimization [66] and make the manufacture process difficult. Therefore, we define area spanned by metallization as

$$A_i(\mathbf{t}_i) = \mathbf{a}^{\mathrm{T}} \mathbf{t}_i, \tag{3.26}$$

where $\mathbf{a} \in \mathbb{C}^{T \times 1}$ is a vector containing area of each discretization element (triangle). Relative area spanned by the metallization $A_{\mathrm{rel}} \in [0, 1]$ can be defined as

$$A_{\mathrm{rel}}(\mathbf{t}_i) = \frac{\mathbf{a}^{\mathrm{T}} \mathbf{t}_i}{\mathbf{a}^{\mathrm{T}} \mathbf{t}_0}, \tag{3.27}$$

and relates the area of metallization corresponding to $\mathbf{t}_i$ to the area of the maximal optimization region Ω_0 corresponding to $\mathbf{t}_0$.

The second geometrical metric deals with shape's regularity. The incidence matrix $\mathbf{M}$ is used to define the triangle connectivity matrix

$$\mathbf{H} = \mathcal{B}(\mathbf{M}\mathbf{M}^{\mathrm{T}}), \tag{3.28}$$

and the rows of the triangle connectivity matrix are further normalized as

$$\hat{\mathbf{H}} = \left[\frac{\mathbf{h}_1}{\|\mathbf{h}_1\|_1} \quad \cdots \quad \frac{\mathbf{h}_T}{\|\mathbf{h}_T\|_1} \right]^{\mathrm{T}}, \tag{3.29}$$

with $\|.\|_p$ being p-th norm [67]. The regularity of a shape $\mathbf{t}_i$ is then expressed as

$$h(\mathbf{t}_i) = 1 - \frac{1}{T} \left\| \mathbf{t}_0 - 2\hat{\mathbf{H}}\mathbf{t}_i \right\|_1, \tag{3.30}$$

which counts enabled/disabled triangles connected to each triangle, *i.e.*, $h \in [0, 1]$. The value $h = 0$ corresponds to the most regular shapes: a region Ω_0 completely filled by metallization ($\mathbf{t}_i = \mathbf{t}_0$) or completely empty ($\mathbf{t}_i = \neg \mathbf{t}_0$). The value $h = 1$ indicates the worst possible case, in which one half of all neighboring triangles is enabled. Particular values of geometry-related metrics are depicted in figure 3.8 for a few shapes.
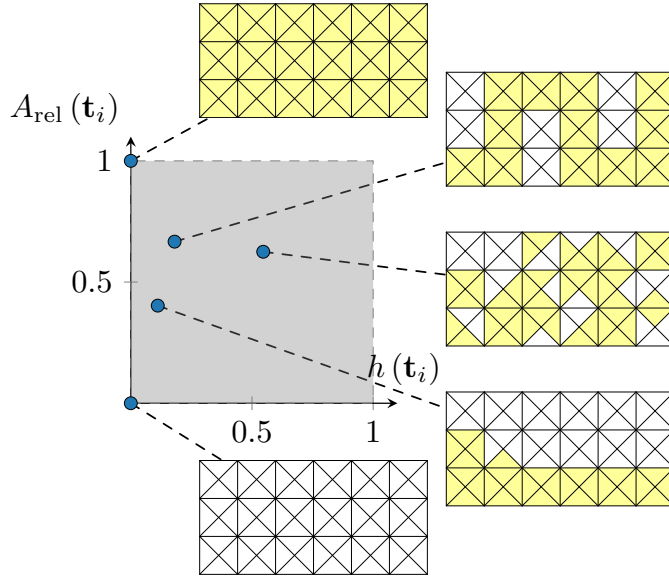
Figure 3.8: Geometrical metrics, *i.e.*, regularity h and area spanned by metallization, for a few shapes represented by the binary vector $\mathbf{t}_i$. The enabled and disabled triangles are depicted by yellow and white color, respectively.

29

Chapter 4

Implementation

In this chapter, the procedures developed earlier are implemented in MAT-LAB[1]. Vectorization [68] of removal/addition formulas for current accumulation (3.22) after every possible shape perturbation is introduced. Computational complexities of developed vectorized formulas are compared to the naive implementation using `for`-cycle. Afterwards, the implemented memetic algorithm is described in section 4.2.

4.1 MATLAB-like vectorization of topology sensitivity evaluation

The presented algorithm bears many implementation challenges, particularly for triangular discretization with overlapping basis functions (SMoM with RWG), since symmetric blocks $\mathbf{C}^\mathrm{T}\mathbf{Y}\mathbf{C}$ in the (3.20) are not equally sized, *i.e.*, a triangle can be composed up to three basis functions.

Let us start investigating the analytical formula for a 3×3 matrix inversion

$$\mathbf{A}^{-1} = \begin{pmatrix} a & b & c \\ d & e & f \\ g & h & k \end{pmatrix}^{-1} = \frac{1}{\det(\mathbf{A})} \begin{pmatrix} ek - fh & ch - bk & bf - ce \\ fg - dk & ak - cg & cd - af \\ dh - eg & bg - ah & ae - bd \end{pmatrix}, \quad (4.1)$$

with $\det(\mathbf{A})$ being determinant of matrix $\mathbf{A}$

$$\det(\mathbf{A}) = a(ek - fh) - b(dk - fg) + c(dh - eg). \quad (4.2)$$

Formula (4.1) enables evaluation of all symmetric 3×3 block inversions $(\mathbf{C}^\mathrm{T}\mathbf{Y}\mathbf{C})^{-1}$ at once. All inversions are described by a set of six vectors since blocks can be sorted according to figure 4.1. Consequently, all multiplication in (4.1) is performed element-wisely, obtaining six vectors representing matrix elements of an inverted block. This is a valid approach for non-overlapping basis functions since a block's size is always fixed. How to generalize it for overlapping basis functions?

---

[1]Note that different programming language will require a slightly different approach.
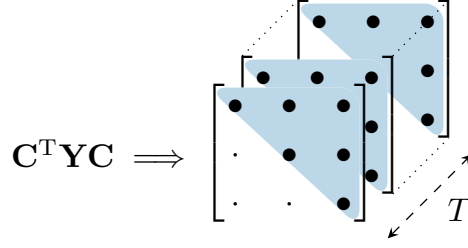
Figure 4.1: Effective rearrangement of investigated 3×3 slices into the third dimension enabling utilization of analytical inversion formula.

Note that formula (4.1) can be reduced to an analytical formula for 2×2 matrix if $c = f = g = h = 0$, $k = 1$ (similar for 1×1 matrix). Discretization with overlapping basis functions does not ensure fixed size of a block for every mesh element, *e.g.*, a triangle can be composed of up to three basis functions. Therefore, we introduce dummy basis function which ensures all blocks to be sized 3×3 resulting in extension of electromagnetic quantities $(\mathbf{Y}, \mathbf{I})$ as

$$\mathbf{Y} = \begin{pmatrix} \mathbf{Y} & \mathbf{0} \\ \mathbf{0}^{\mathrm{T}} & 1 \end{pmatrix}, \tag{4.3}$$

$$\mathbf{I} = \begin{pmatrix} \mathbf{I} \\ 0 \end{pmatrix}. \tag{4.4}$$

Consequently, every mesh element consisting of less than three basis functions is extended by this dummy basis function, effectively enabling vectorization of $(\mathbf{C}^{\mathrm{T}}\mathbf{Y}\mathbf{C})^{-1}$, but not affecting the physical response of the system.

The matrices $\mathbf{M}^{\pm}$ defined in section 3.3 readily provides MATLAB-compatible indexation vector $\mathbf{v}$ of all possible triplets, *e.g.*, for RWG as

$$\mathbf{M}^{-} = \begin{pmatrix} 1 & 1 & 0 & 1 & \cdots & 0 \\ 0 & 1 & 1 & 0 & & 0 \\ 0 & 0 & 1 & 0 & & 0 \\ \vdots & & & & \ddots & \vdots \\ 0 & 0 & 0 & 0 & \cdots & 1 \end{pmatrix} \implies \mathbf{v} = \begin{bmatrix} 1 & 2 & 4, & 2 & 3 & 0, & 3 & 0 & 0, \cdots \end{bmatrix}^{\mathrm{T}}. \tag{4.5}$$

Indexation vector $\mathbf{v}$ can be obtained by performing function `find(.)` row-wisely, which simply transfer positions of logical ones into triplets of fixed size. Extension (4.4) is considered, effectively substituting every zero in the list $\mathbf{v}$ by a $N + 1$ index. The vectorization of removal formula (3.20) is further presented. Vector indexing is performed MATLAB-like via vector $\mathbf{v}$ [69] as

$$\mathbf{C}^{\mathrm{T}}\mathbf{Y}\mathbf{C} \rightarrow \mathbf{Y}(\mathbf{v}, \mathbf{v}) = \begin{pmatrix} \cdot & \cdot & \cdot & & & \\ \cdot & \cdot & \cdot & & & \\ \cdot & \cdot & \cdot & & & \\ & & & \cdot & \cdot & \cdot \\ & & & \cdot & \cdot & \cdot \\ & & & \cdot & \cdot & \cdot \end{pmatrix}, \tag{4.6}$$

where desired 3×3 blocks form block-diagonal matrix. All these entries are reshaped to a set of six vectors $\mathbf{s}_{xx} \in \mathbb{C}^{1 \times 1 \times T}$ according to figure 4.1 and all blocks are inverted at once

$$(\mathbf{C}^\mathrm{T}\mathbf{Y}\mathbf{C})^{-1} = \begin{pmatrix} \mathbf{s}_{11} & \mathbf{s}_{12} & \mathbf{s}_{13} \\ \mathbf{s}_{12} & \mathbf{s}_{22} & \mathbf{s}_{23} \\ \mathbf{s}_{13} & \mathbf{s}_{23} & \mathbf{s}_{33} \end{pmatrix}^{-1} = \begin{pmatrix} \mathbf{b}_{11} & \mathbf{b}_{12} & \mathbf{b}_{13} \\ \mathbf{b}_{12} & \mathbf{b}_{22} & \mathbf{b}_{23} \\ \mathbf{b}_{13} & \mathbf{b}_{23} & \mathbf{b}_{33} \end{pmatrix} = \mathbf{B}, \qquad (4.7)$$

obtaining a matrix $\mathbf{B} \in \mathbb{C}^{3 \times 3 \times T}$, *i.e.*, all inverted blocks are represented by 6 vectors $\mathbf{b}_{xx} \in \mathbb{C}^{1 \times 1 \times T}$. Current product $\mathbf{C}^\mathrm{T}\mathbf{I}$ is also divided into triplets reshaped similarly like in figure 4.1

$$\mathbf{C}^\mathrm{T}\mathbf{I} \to \mathbf{I}(\mathbf{v}) = \begin{pmatrix} . \\ . \\ . \\ \\ . \\ . \\ . \end{pmatrix} \implies \begin{pmatrix} \mathbf{I}_1 \\ \mathbf{I}_2 \\ \mathbf{I}_3 \end{pmatrix} = \mathbf{I}_m \qquad (4.8)$$

where a slice of vector $\mathbf{I}_m \in \mathbb{C}^{3 \times 1 \times T}$ represents current flowing through basis functions of m-th mesh element. Multiplication is performed element-wise (for each block separately) as

$$(\mathbf{C}^\mathrm{T}\mathbf{Y}\mathbf{C})^{-1}\mathbf{C}^\mathrm{T}\mathbf{I} \to \begin{pmatrix} \mathbf{b}_{11} & \mathbf{b}_{12} & \mathbf{b}_{13} \\ \mathbf{b}_{12} & \mathbf{b}_{22} & \mathbf{b}_{23} \\ \mathbf{b}_{13} & \mathbf{b}_{23} & \mathbf{b}_{33} \end{pmatrix} \begin{pmatrix} \mathbf{I}_1 \\ \mathbf{I}_2 \\ \mathbf{I}_3 \end{pmatrix} = \sum_{\text{rows}} \mathbf{B} \odot \mathbf{I}_m^\mathrm{T}, \qquad (4.9)$$

where the final product of size $3 \times 1 \times T$ is reshaped into $3T \times 1$ vector $\mathbf{I}_B$. MATLAB-like notation of left indexing is performed, obtaining triplets of columns as

$$\mathbf{Y}\mathbf{C} \to \mathbf{Y}(:, \mathbf{v}) = \begin{pmatrix} . & . & . & & . & . & . \\ . & . & . & & . & . & . \\ . & . & . & & . & . & . \\ . & . & . & & . & . & . \\ . & . & . & & . & . & . \\ . & . & . & & . & . & . \end{pmatrix}, \qquad (4.10)$$

and multiplied element-wise

$$\mathbf{Y}(:, \mathbf{v}) \odot \mathbf{I}_B^\mathrm{T} = \begin{pmatrix} . & . & . & & . & . & . \\ . & . & . & & . & . & . \\ . & . & . & & . & . & . \\ . & . & . & & . & . & . \\ . & . & . & & . & . & . \\ . & . & . & & . & . & . \end{pmatrix} \implies [\mathbf{I}_p] \qquad (4.11)$$

Matrix product $[\mathbf{I}_p]$ is evaluated by summing triplets in the matrix in (4.11) row-wisely, effectively obtaining a matrix of size $N \times T$, where each column

represents a correction to the current $\mathbf{I}$ flowing onto the actual shape, which is being investigated for structural perturbations. With the implicit expansion of dimension in MATLAB, the perturbed current accumulated into a matrix in (3.20) is evaluated as

$$[\hat{\mathbf{I}}] = \mathbf{I} - [\mathbf{I}_p],\tag{4.12}$$

which is fully compatible with topology sensitivity evaluation (3.23). The evaluation of removal formula (3.20) is much faster than evaluation based on scripted-loop. The maximal speedup is nearly 110, see figure 4.2, for a shape composed of T discretization elements, in which every element is investigated for removal except two of them representing fixed and predetermined feeding.
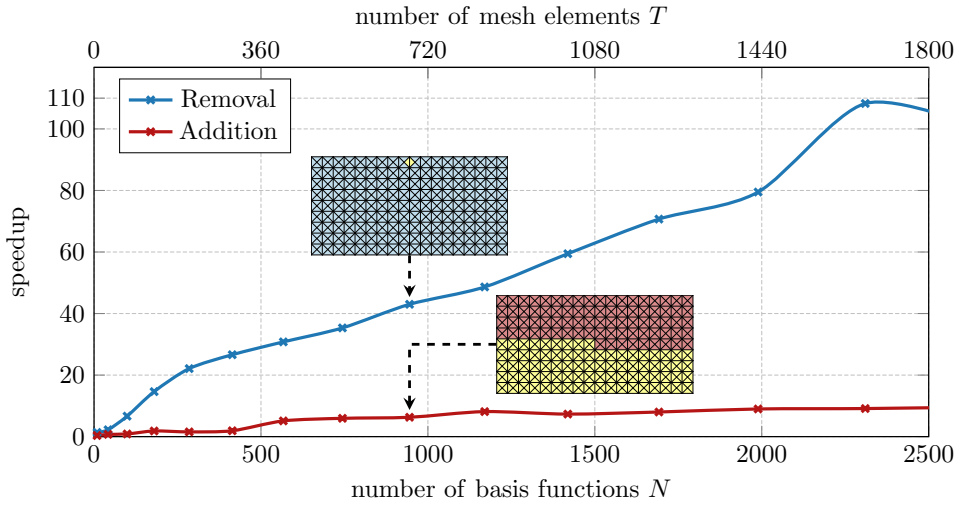
Figure 4.2: Speedup of vectorized removal formula (3.20) and addition formula (3.21) compared to the code based on scripted loops. All blue and red triangles are tested for removal and addition, respectively. The yellow color depicts fixed triangles that are not tested.

The idea behind vectorization of addition formula (3.21) remains the same. The triplets are stacked across the third dimension, effectively turning standard matrix multiplication into element-wise. The vectorized addition formula requires more operation than the removal formula. Therefore, it is computationally more expensive, reaching a speedup of almost 10, see figure 4.2. Since we assume only boundary triangles to be tested for addition, the tested addition set is likely to be much smaller than the tested removal set. Therefore, the majority of the computational time is spent evaluating the removals.

▮ 4.2 Algorithm description

Structural perturbation according to the topology sensitivity (3.23) to reach the local optimum of an antenna metric p can be understood as a discrete version of a greedy gradient-based algorithm [7]. Since the gradient-based

algorithms do not ensure convergence to the global optimum, it is combined with the global optimization technique and forms a memetic algorithm [70]. Genetics used in this work is a single-objective genetics algorithm (SOGA) [71].

The memetic algorithm is further implemented in MATLAB [69] using AToM package [55] and FOPS package [72]. MATLAB provides an efficient implementation of matrix manipulations and matrix indexing.

The flowchart of the implemented memetic algorithm is depicted in figure 4.3. An antenna model, *i.e.*, the mesh of the region (Ω_T), electrical size (ka), feeding ($\mathbf{V}$), and antenna metric to be optimized (p), is defined first. The impedance matrix $\mathbf{Z}$ is further computed together with necessary matrices used for antenna metric p evaluation. In the next step, the optimization procedure combining global and local step in a memetic sense begins.

The global step operates with a set of agents, in which every agent repeats the local step. At the end of each iteration of the global step, the genetic operators are employed on locally optimal shapes. This cycle is repeated until a maximum number of iterations I is reached[2]. Every iteration is initiated with a random seed of design variables represented by a vector $\mathbf{t}_i$. The initial impedance matrix $\mathbf{Z}$ is truncated according to initial shape $\mathbf{t}_i$ and inverted. Afterwards, the current is evaluated for the predefined excitation vector $\mathbf{V}$.

The core of the algorithm, the local step based on topology sensitivity, is initiated for every candidate proposed by the global step. The tested sets of candidates for removals and additions represented by matrices $\mathbf{M}^{\pm}$ are firstly determined in order to obtain information about tested mesh elements. Perturbation currents $[\hat{\mathbf{I}}]^{\pm}$ are evaluated according to vectorized formulas described in section 4.1. Consequently, the topology sensitivity $\boldsymbol{\tau}$ (3.23) is evaluated via exact re-analysis without the necessity of inverting the actual impedance matrix. It computes the improvement in terms of antenna metric p for every perturbation. The best possibility is chosen in each step, *i.e.*, greedy algorithm [6] is performed. The shape is updated in terms of geometrical $\mathbf{t}_i$ and physical $\hat{\mathbf{Y}}, \hat{\mathbf{I}}$ quantities and the local step is iteratively repeated until the termination criterion is satisfied, *i.e.*, when the local optimum is reached. If the maximum number of iteration I is reached, the optimal shape Ω^* guarantees a good optimal value of the antenna metric p^*.

---

[2]There are other termination criteria available, *e.g.*, the maximum relative error between two iterations.
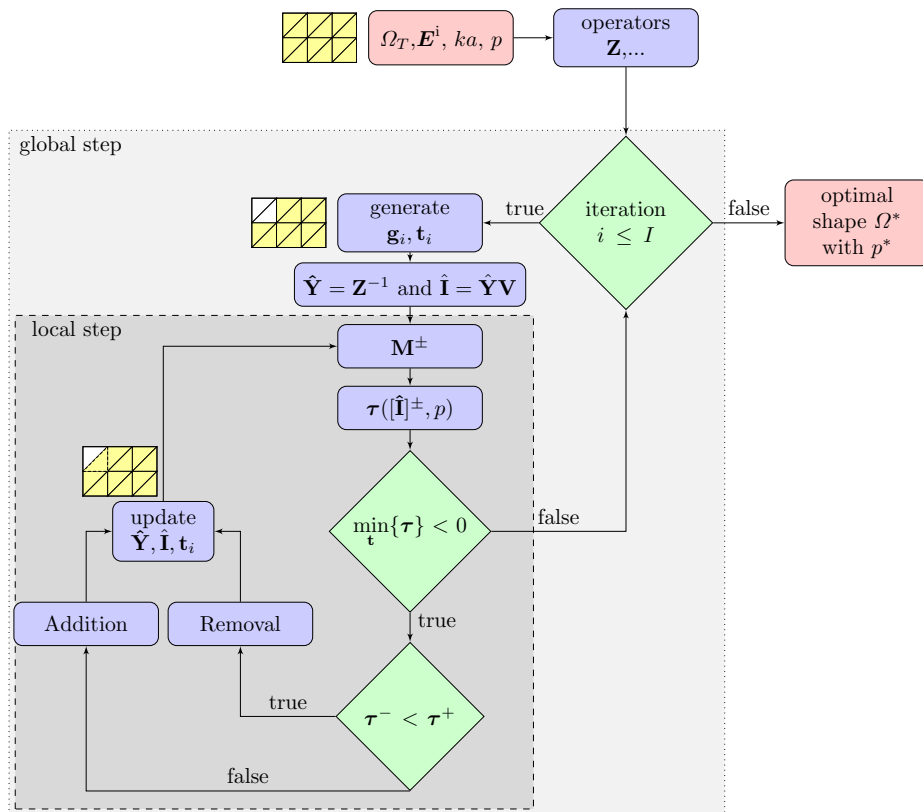
Figure 4.3: A flowchart of the implemented memetic algorithm with a local step based on the topology sensitivity with exact re-analysis.

Chapter 5

Examples

In this chapter, the developed memetic algorithm based on mesh elements perturbation scheme is employed on several examples demonstrating its capabilities. Comparison of the scheme based on mesh elements and its predecessor based on manipulation with basis functions, see section 2.2.4, is also made. All computations are performed on a computer cluster at Research Center for Informatics (RCI) [73] which is available for students of Faculty of Electrical Engineering in Czech Technical university in Prague. RCI cluster is a High Performance Computing (HPC) infrastructure that provides 33 computing nodes, each of which consists of 24 physical cores ($2\times$ Intel Xeon Scalable Gold 6146, 3.2 GHz, 384 GB RAM). One computing node was used for all the evaluations in this thesis.

5.1 Radiation Q-factor

Q-factor is an important parameter of electrically small antennas due to its inverse proportionality to the fractional bandwidth (FBW) [50].

Q-factor is defined in a standard fashion [74]. Using impedance matrix $\mathbf{Z} = \mathbf{R} + \mathbf{R}_\rho + \mathrm{j}\mathbf{X}$ and stored energy matrix $\mathbf{W} = \omega\partial\mathbf{X}/\partial\omega$, the so-called tuned Q-factor is defined as

$$Q = Q_\mathrm{U} + Q_\mathrm{ext} = \frac{4\omega\max\{W_\mathrm{m}(\mathbf{I}), W_\mathrm{e}(\mathbf{I})\}}{\mathbf{I}^\mathrm{H}\mathbf{R}\mathbf{I}}, \tag{5.1}$$

where untuned part is

$$Q_\mathrm{U} = \frac{\omega W_\mathrm{sto}}{P_\mathrm{rad}} = \frac{\mathbf{I}^\mathrm{H}\mathbf{W}\mathbf{I}}{2\mathbf{I}^\mathrm{H}\mathbf{R}\mathbf{I}}, \tag{5.2}$$

and where external (matching) part Q_ext [75] is

$$Q_\mathrm{ext} = \frac{|\mathbf{I}^\mathrm{H}\mathbf{X}\mathbf{I}|}{4\mathbf{I}^\mathrm{H}\mathbf{R}\mathbf{I}}, \tag{5.3}$$

where radiated power

$$P_\mathrm{rad} = \frac{1}{2}\mathbf{I}^\mathrm{H}\mathbf{R}\mathbf{I}, \tag{5.4}$$

is substituted. External Q-factor measures the stored energy of a thought external lumped reactance required to tune system into the resonance if this is not achievable by shaping the current density itself, *i.e.*, by so-called self-resonance $\mathbf{I}^{\mathrm{H}}\mathbf{XI} = 0$.

Developed optimization algorithm cannot enforce equality constraints such as $\mathbf{I}^{\mathrm{H}}\mathbf{XI} = 0$. Therefore, we introduce coefficient $\alpha \geq 1$ which penalizes non-zero values of external Q-factor forming a swept optimization problem

$$
\begin{aligned}
\min_{\mathbf{t}_i} \quad & Q(\mathbf{I}) = Q_{\mathrm{U}}(\mathbf{I}) + \alpha Q_{\mathrm{ext}}(\mathbf{I}), \\
\text{s.t.} \quad & \mathbf{I}(\mathbf{g}_i) = \mathbf{Z}(\mathbf{g}_i)^{-1}\mathbf{V}, \\
& \mathbf{g}_i = \neg\mathcal{B}\left(\mathbf{M}^{\mathrm{T}}\mathbf{t}_i - 2\right), \\
& \mathbf{t}_i \in \{0,1\}^N.
\end{aligned}
\tag{5.5}
$$

in which we can choose the preference between self-resonant current density and low value of Q-factor.

One local step of the memetic algorithm from section 4.2 is employed on problem (5.5). The considered setup consists of a PEC plate with $2:1$ aspect ratio, which is uniformly discretized into 128 triangles and 180 basis functions at electrical size $ka = 0.5$. A delta gap source is placed in the top center, see (A) in figure 5.1 of the plate. The optimized metric Q is further normalized to the fundamental bound $Q_{\mathrm{lb}} = 35.4$ (simultaneous TM and TE operation) [76] which presents the absolute lower bound to Q-factor. The optimal shape found via topology sensitivity algorithm with penalty coefficient $\alpha \geq 1.1$ resulting in self-resonant current density is shown in panel (B) in figure 5.1 reaching normalized Q-factor $Q/Q_{\mathrm{lb}} = 2.01$. The corresponding current distribution is depicted in panel (C) of the same figure. Panel (D) in figure 5.1 shows a map of topology sensitivity τ for all possible removals and additions in the third iteration of the optimization algorithm. Removing triangles with positive values of topology sensitivity lowers the optimized metric, *e.g.*, the triangle highlighted by the green color is to be removed at this step. Removal of this triangle causes a drop in optimized metric from $Q/Q_{\mathrm{lb}} = 14.88$ to $Q/Q_{\mathrm{lb}} = 3.90$. The reason for this remarkable improvement is that the structure is effectively separated, the electric short is removed, and the structure starts to separate electric charge well, which is the main goal when Q-factor of an electrically small antenna is minimized (*i.e.*, to maximize polarizability of the structure [77]).

The described greedy algorithm is deterministic, and the optimized metric always ends in the same local optima for the same initial shape. For that reason, the full memetic algorithm from figure 4.3 is performed next on a finer mesh to obtain Q-factor even closer to the lower bound.

Consider the same PEC plate uniformly discretized into 512 triangles and 744 basis functions at the same electrical size $ka = 0.5$ and with the same feeding. In this particular example, we consider normalization of Q-factor to the fundamental bound $Q_{\mathrm{lb}}^{\mathrm{TM}}$ [76] generated by TM modes only since for this particular excitation, and only TM modes can effectively be excited. Furthermore, the memetic algorithm is employed on (5.5) using both mesh
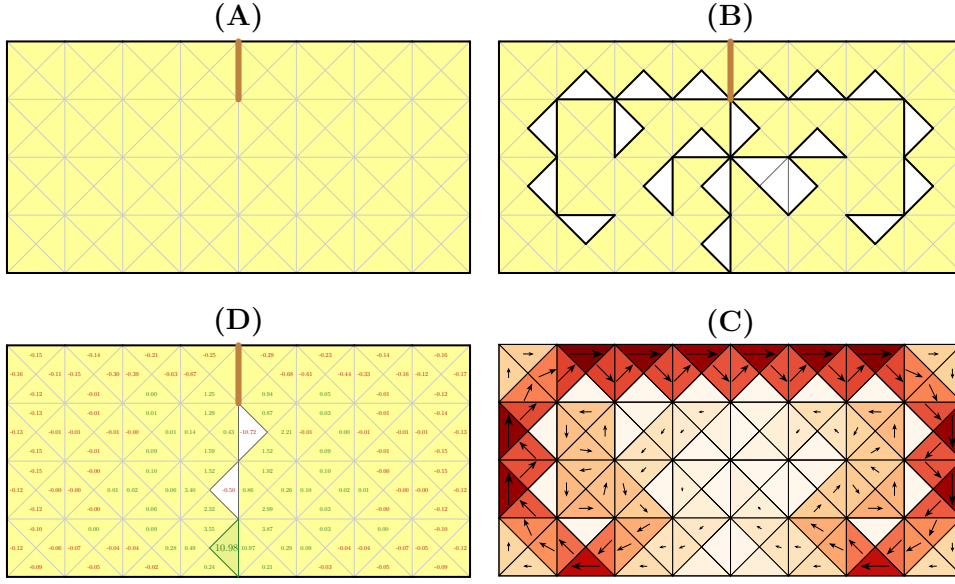
$i = 3 \rightarrow Q/Q_{\mathrm{lb}} = 14.88$

Figure 5.1: (A) A uniformly discretized PEC plate with aspect ratio $2 : 1$ and electrical size $ka = 0.5$, where k is the wavenumber and a is the radius of the smallest circumscribing sphere. The feeding is realized by a discrete delta gap source highlighted by the brown color. (B) Optimal shape found via topology sensitivity algorithm. (C) The optimal current distribution is reaching $Q/Q_{\mathrm{lb}} = 2.01$. (D) Topology sensitivity map determining topology sensitivity τ for each triangle in the third step of greedy algorithm. If the triangle highlighted by the green color is removed, the normalized Q-factor Q/Q_{lb} is improved from the initial value 10.98 to $Q/Q_{\mathrm{lb}} = 3.90$.

elements and basis functions [12] in order to compare both schemes in terms of realized Q-factors.

Consequently, the optimization task (5.5) is also extended by introducing geometrical metrics, see section 3.8, as

$$
\begin{aligned}
\min_{\mathbf{t}_i} \quad & Q(\mathbf{I}) = Q_{\mathrm{U}}(\mathbf{I}) + \alpha Q_{\mathrm{ext}}(\mathbf{I}) + \beta A_{\mathrm{rel}}(\mathbf{t}_i) + \gamma h(\mathbf{t}_i), \\
\text{s.t.} \quad & \mathbf{I}(\mathbf{g}_i) = \mathbf{Z}(\mathbf{g}_i)^{-1}\mathbf{V}, \\
& \mathbf{g}_i = \neg \mathcal{B}\left(\mathbf{M}^{\mathrm{T}}\mathbf{t}_i - 2\right), \\
& \mathbf{t}_i \in \{0, 1\}^N,
\end{aligned}
\tag{5.6}
$$

and the optimal shape is obtained by the memetic algorithm with triangle perturbation scheme for a fixed values of constants in (5.6), *i.e.*, $\beta = 0.4$, $\gamma = 0.25$.

The results are depicted in figure 5.2. Two sets of markers are introduced, non-dominated and dominated solutions. Non-dominated solutions form the Pareto-optimal set [18]. Penalty α is used to enforce the self-resonance ($Q_{\mathrm{ext}} = 0$). The vertical shift between both perturbation paradigms is obvious. The mesh elements perturbation scheme (easily geometrically interpreted)

39

pays the price in terms of realized physical quantities, *i.e.*, $Q/Q_\mathrm{lb}^\mathrm{TM}$, as opposed to the basis function perturbation scheme, which realizes physical quantities closer to the bound.

Introducing geometrical metrics into the optimization causes that non-dominated solutions are more vertically shifted, paying the price for realizing more regular shapes. The effect of geometrical metrics is directly visible from the realized shapes, *e.g.*, removal of solitary triangles is enforced by A_rel, which impose requirements on the amount of metallization. Realization of self-resonant shapes is still possible, but at a higher cost in terms of Q_U. Optimization of a finer discretization will most likely result in a negligible difference between the optimized metric of both schemes.
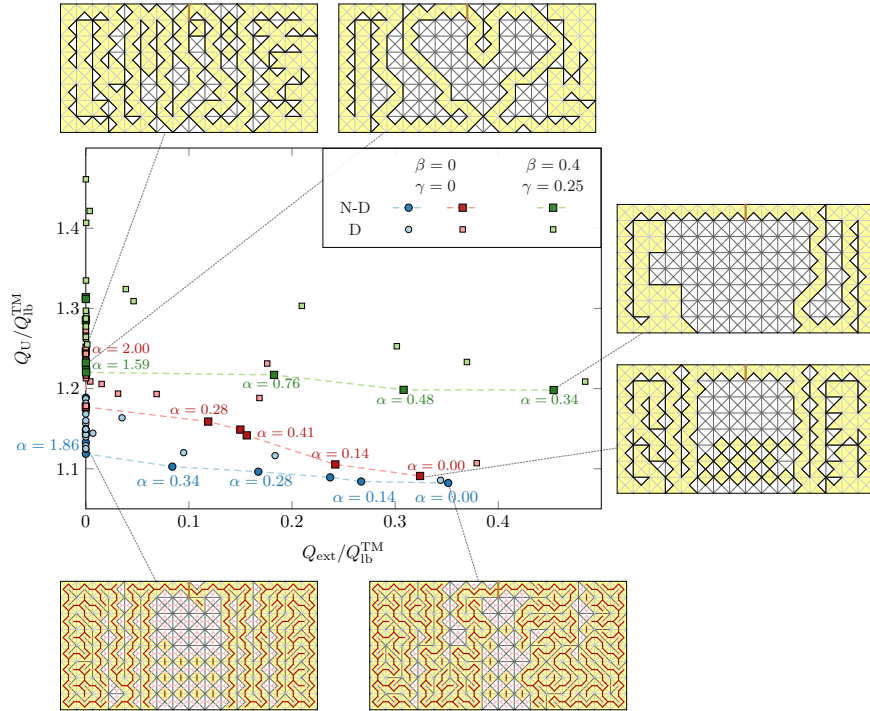
Figure 5.2: Q-factor minimization (5.6) of a structure carved into a PEC plate with $2:1$ aspect ratio at electrical size $ka = 0.5$. The memetic algorithm based on both perturbation schemes (triangles × basis functions) is used with 96 agents and 400 iterations with relative maximal relative error for all agents between two iterations lower than 10^{-9} for the global step. Different values of weights α, β, γ denotes preferences with respect to self-resonance, used area and regularity, respectively. The x-axis can span values from 0 to 1 and the y-axis from 1 to infinity due to the normalization to $Q_\mathrm{lb}^\mathrm{TM}$. The blue circle markers denote the basis function perturbation scheme without geometrical constraints, while the square markers depict optimization based on triangles. The red square denotes optimization without geometrical requirements. The label "N-D" stands for "non-dominated" points, and the label "D" stands for "dominated" points [18]. Non-dominated solutions are interconnected by a dashed line to approximate Pareto optimal set.

Finally, we investigate the computational complexity of both versions
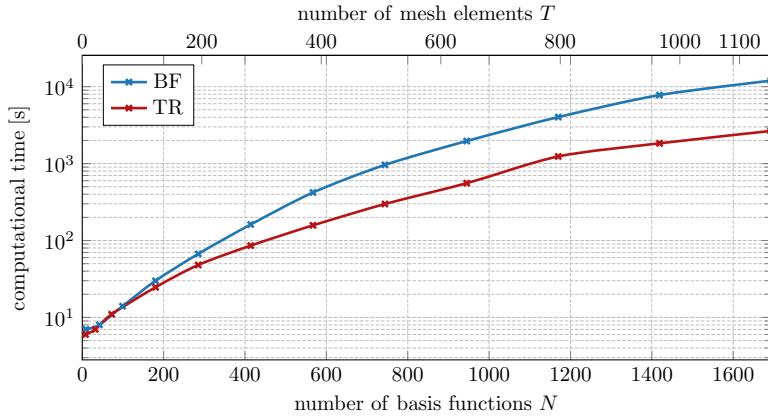
Figure 5.3: The computational complexity of the full memetic algorithm based on triangles (TR) and basis functions (BF) for varying number of triangles T and corresponding number of basis functions N.

of the memetic algorithm, *i.e.*, based on basis functions and mesh element perturbation schemes. The optimization task (5.5) is performed for various uniformly discretized plates (up to a plate made of 12×24 pixels) with a fixed value of alpha. All computations were evaluated on RCI cluster with 48 agents and 100 iterations in 5 separate runs. Figure 5.3 presents resulting average computational complexity. It is observed that reduction of solution space in the case triangular scheme results in lower computational time. Figure 5.2, however, shows that it is at the cost of realized Q-factor. Nevertheless, finer discretization can be employed, resulting in better performance of an optimal shape. The vertical shift of both curves is most likely to monotonically grow, making mesh element based optimization more effective in terms of computational time for large-scale structures.

5.2 Total efficiency

Total efficiency as a combination of matching efficiency η_{match} and radiation efficiency η_{rad} is also an important parameter of electrically small antennas, comparing the cycle mean power delivered to the input port with the cycle mean power radiated by the antenna. This parameter takes into account both the power dissipated in thermal loss and reflections due to the impedance mismatch, see figure 5.4. For simplicity, loss-less matching circuitry is assumed in this example. The total efficiency η is defined as

$$\eta = \eta_{\mathrm{match}}\eta_{\mathrm{rad}} = \left(1 - |\Gamma|^2\right) \frac{P_{\mathrm{rad}}}{P_{\mathrm{rad}} + P_{\mathrm{lost}}} = \left(1 - |\Gamma|^2\right) \frac{1}{1 + \delta}, \qquad (5.7)$$

where P_{rad} and P_{lost} are cycle mean radiated and ohmic lost power, respectively, Γ is reflection coefficient [2] and $\delta = P_{\mathrm{lost}}/P_{\mathrm{rad}}$ is the dissipation factor [78]. Within MoM paradigm the radiated power and ohmic losses are

evaluated as

$$P_{\mathrm{rad}} \approx \frac{1}{2}\mathbf{I}^{\mathrm{H}}\mathbf{R}\mathbf{I}, \tag{5.8}$$

$$P_{\mathrm{lost}} \approx \frac{1}{2}\mathbf{I}^{\mathrm{H}}\mathbf{R}_{\rho}\mathbf{I}. \tag{5.9}$$
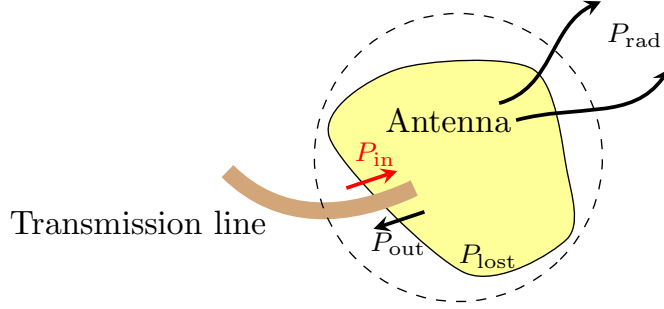
Figure 5.4: An illustration of the power balance of a transmitting antenna. The input power P_{in} equals the summation of the radiated power P_{rad}, reflected power P_{out} and thermal losses P_{lost}.

Analogously to previous section, the maximization of the total efficiency η with geometrical constraints included is defined as

$$
\begin{aligned}
\min_{\mathbf{t}_i} \quad & -\frac{1}{N_f}\sum_{n=1}^{N_f}\eta_n + \beta A_{\mathrm{rel}}(\mathbf{t}_i) + \gamma h(\mathbf{t}_i), \\
\text{s.t.} \quad & \mathbf{I}(\mathbf{g}_i) = \mathbf{Z}(\mathbf{g}_i)^{-1}\mathbf{V}, \\
& \mathbf{g}_i = \neg\mathcal{B}\left(\mathbf{M}^{\mathrm{T}}\mathbf{t}_i - 2\right), \\
& \mathbf{t}_i \in \{0,1\}^N,
\end{aligned}
\tag{5.10}
$$

where N_f is the number of target frequencies.

The optimization task (5.10) is performed on $0.21\,\mathrm{m} \times 0.20\,\mathrm{m}$ sized PEC plate which is uniformly discretized into 21 pixels $\times$ 20 pixels, *i.e.*, into 1680 triangles and 2479 basis functions. The feeding is realized using a delta gap source in the middle of the plate. The input impedance of the antenna should be matched to $50\,\Omega$. The surface impedance is set to $0\,\Omega/\mathrm{m}^2$. The target frequencies are set to $370\,\mathrm{MHz}$ and $420\,\mathrm{MHz}$. Following optimizations are performed with weights for geometrical metrics $\beta = 0.25$ and $\gamma = 0.25$ to regularize the resulting structure.

The total efficiency maximization is firstly performed by the local step of the implemented algorithm, with an initial shape being with all triangles enabled. The optimal shape was obtained after 478 iterations with about 550 seconds of computation time. The optimization task was also performed by the full memetic algorithm with 48 agents and 200 iterations. The corresponding optimal shape was obtained in 2100 seconds. The total efficiency of optimal designs obtained by both approaches, mentioned earlier, is compared to the
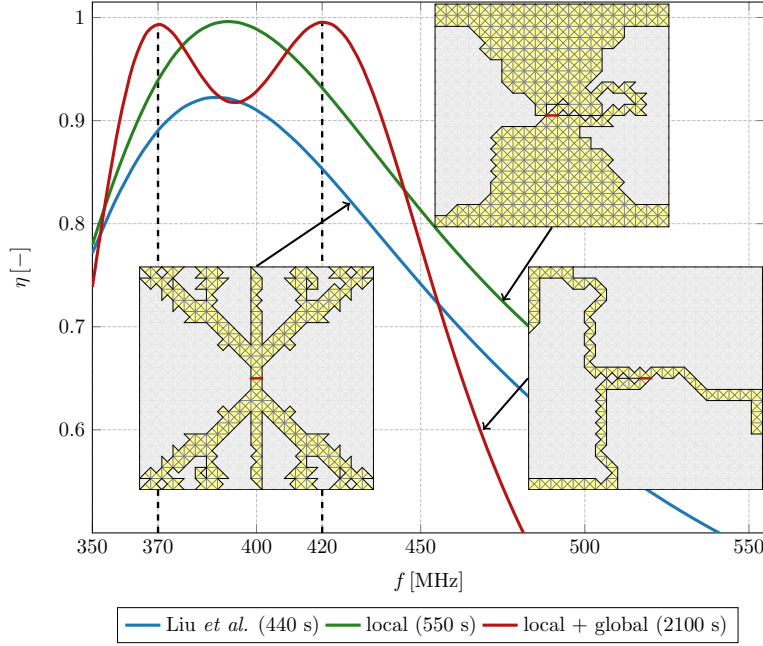
Figure 5.5: Total efficiency obtained by the topology optimization algorithm based on MoM (blue), see section 2.2.3, compared to the total efficiency received by employing only local (green) and global (red) step of the implemented algorithm.

total efficiency of design obtained by Liu *et al.* [44], see section 2.2.3, and the comparison is presented in figure 5.5.

The optimization was also investigated in terms of computational efficiency and the value of the optimized metric. The comparison of three different optimization solvers is performed with the same optimization prerequisites as in the previous paragraph. The structure was firstly optimized by the local step, *i.e.*, topology sensitivity algorithm, for the random initial shape. The structure was then optimized by a robust genetic algorithm, *i.e.*, "classical" pixeling scheme [13] in which MoM is repetitively employed. Lastly, the combination of heuristics and topology sensitivity, *i.e.*, the developed memetic algorithm, is also performed. Ten runs of each computational scheme were made, and figure 5.6 presents resulting envelopes for computational time and antenna performance trade-offs, *i.e.*, it shows a realizable optimized metric value in a particular computational time for each solver. It is clear that a combination of genetic and local algorithm combines good properties of both approaches; computation speed of local algorithm and robustness of the genetic algorithm.

The optimization task was also repeated for stainless steel with electric conductivity $\sigma = 1.45 \times 10^6$ S/m in order to be closer to the realizable antenna, which is to be realized by cutting into a metallic sample made of stainless steel. Maximization of total efficiency (5.10) with same weights for the geometric metrics and at same target frequencies as in the previous
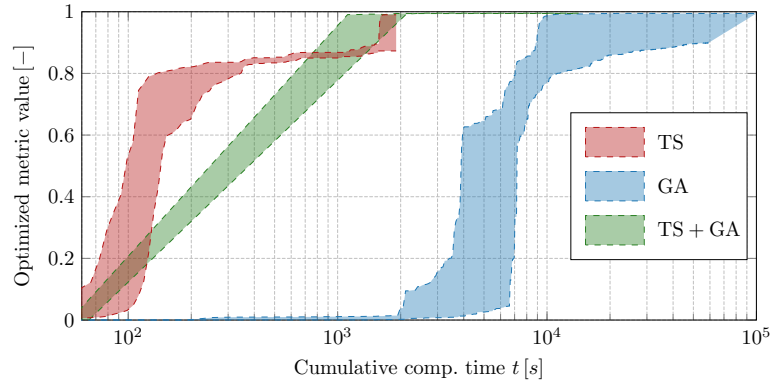
Figure 5.6: Optimization task (5.10) is performed by three different solvers; topology sensitivity (TS) as a local step, pure genetic algorithm (GA) and their combination. All solvers perform ten separate runs for different initial shapes. The results, therefore, form shaded regions with envelopes depicted by dashed lines. The optimized metric is the mean value of total efficiency at target frequencies from (5.10).

paragraph is performed, forming two dipole-like sheets of different length, *i.e.*, path in which current resonates at the target frequencies, see figure 5.7. The red curve illustrates the addition of the third target frequency, which causes the creation of another dipole-like current path.
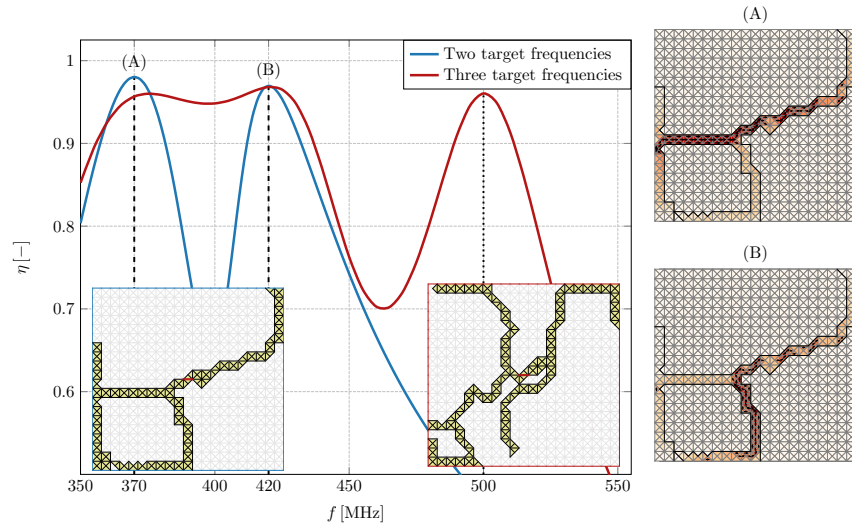
Figure 5.7: Antenna structures obtained by the proposed algorithm with an assumption on stainless steel used as a conductor. Two dipole-like paths resonate at each target frequency (A) and (B). Addition of the third target frequency results in the creation of a third dipole-like path.

The optimal antenna depicted in bottom left of figure 5.7 which exhibits maximal total efficiency on 370 MHz and 420 MHz was modelled in CST Studio Suite in order to obtain confidence in the evaluated results and approach the manufacturing of this design. In contrast to the previous setup, the

44

feeding region now lies on a slab made of epoxy laminate dielectric substrate IS400 [79] with permittivity $\varepsilon_r = 3.9$, which also carries both metallic parts of the antenna, see figure 5.8. Realistic thickness 0.5 mm of metallization is also introduced. Comparison of total efficiency of the previous and simplified design with the design used in the CST model is presented in figure 5.9 where we directly observe frequency shift caused by the finite thickness of metallic parts and involvement of dielectric substrate. Thus, the design requires manual tuning. The manually tweaked design was manufactured, see inset (B) in figure 5.9, but the feeding region tuning and precise efficiency measurement in the anechoic chamber will be performed later before the thesis defense.
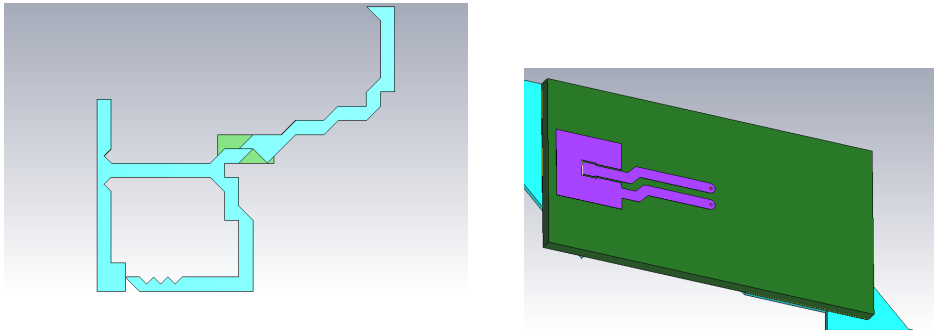
Figure 5.8: The optimized antenna was modelled in CST Studio Suite (left) introducing finite thickness of the metallization. Copper pads for placement of the SMA connector are realized on a dielectric substrate IS400 ($\varepsilon_r = 3.9$) (right). The pads are connected to the metallic parts of the antenna by vias.
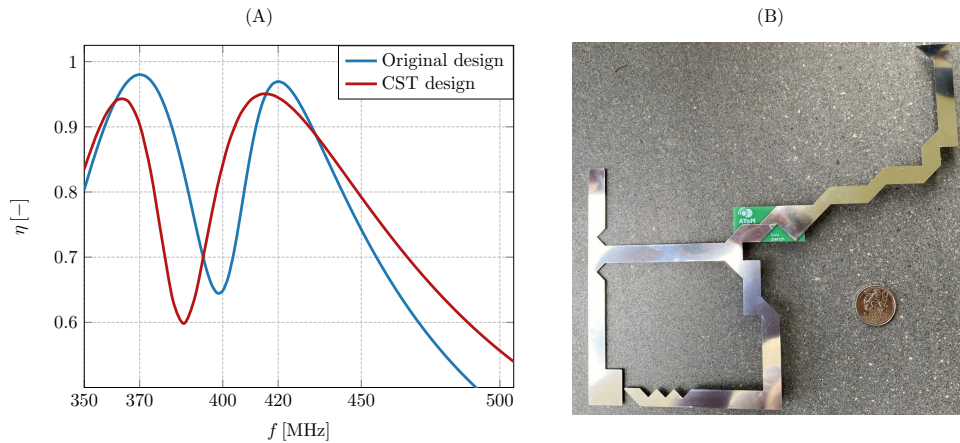
Figure 5.9: (A) Comparison of the total efficiency of optimized design obtained by the developed algorithm on a simplified model (blue curve) and design post-processed in CST Studio Suite (red curve). In contrast to the optimized design, the design analyzed in CST contains dielectric, which provides mechanical support and also contains feeding, which is the major reason for the difference between the curves. The total efficiency was computed via frequency solver with adaptive meshing turned on in order to obtain accurate data. (B) A post-processed model is manufactured by cutting into a metallic sample made of stainless steel.

■ 5.3 Scattering cross section of a dielectric slab

In this section, we study the maximization of scattering cross section σ_{scat} for a volumetric body discretized into a set of tetrahedral elements in order to present the versatility of the implemented algorithm. The scattering cross-section represents the amount of power scattered by the object overpower flux supplied by the incident wave [80]. In the optimization of cross-sections, a fixed incident field $\mathbf{V}$ is considered in the form of a plane wave [81]. Maximization of scattering cross-section is rewritten as a minimization task and reads

$$
\begin{aligned}
\min_{\mathbf{t}_i} \quad & -\sigma_{\text{scat}}(\mathbf{I}) = -\frac{1}{2}\frac{\mathbf{I}^{\text{H}}\mathbf{R}\mathbf{I}}{S_0}, \\
\text{s.t.} \quad & \mathbf{I}(\mathbf{g}_i) = \mathbf{Z}(\mathbf{g}_i)^{-1}\mathbf{V}, \\
& \mathbf{g}_i = \mathbf{M}^{\text{T}}\mathbf{t}_i, \\
& \mathbf{t}_i \in \{0,1\}^N,
\end{aligned}
\tag{5.11}
$$

where the incident field is a plane wave with power flux S_0. The relation between binary vectors $\mathbf{t}_i$ and $\mathbf{g}_i$ is different from the previous section since we assume employment of non-overlapping basis functions with VMoM.

The optimization task (5.11) is attempted by the implemented algorithm based on tetrahedral perturbation scheme and compared to the original version based on basis function perturbation. The figure 5.10 presents realizable maximal scattering cross sections of $2l \times l \times l/5$, $l = 200\,\text{nm}$ slab made of gold [82] at frequency range $f \in [160, 624]\,\text{THz}$ by both versions of the algorithm and is compared to the upper bound [83]. In principle, the algorithm with the tetrahedral element perturbation scheme cannot achieve values found by the algorithm based on basis functions perturbation[1], nevertheless, it offers direct geometrical interpretation and lower computation times, which is also clear from table 5.1. It can also be seen that the reduction of the solution space in the tetrahedral scheme results in lower number of investigated shapes and drop in computation time. More significant drop was nevertheless expected due to the employed vectorization, see section 4.1. Hence, this clearly indicates that the implementation can be further improved.

■ 5.4 PIFA design

In this example we consider a practical example of antenna design. Example covered in this section is inspired by course *Antenna design and construction* (in Czech: Návrh a konstrukce antén) in which we designed a planar inverted F-antenna (PIFA) in electromagnetic simulator CST Studio Suite. The goal was to design an antenna with minimal reflectance $|S_{11}|$ in two frequency bands: $\text{E} - \text{GSM} \in [880, 935]\,\text{MHz}$ and $\text{DCS} \in [1710, 1880]\,\text{MHz}$, with additional specification:

---

[1]Three times fewer degrees of freedom but hard to interpret in terms of geometrical modification.
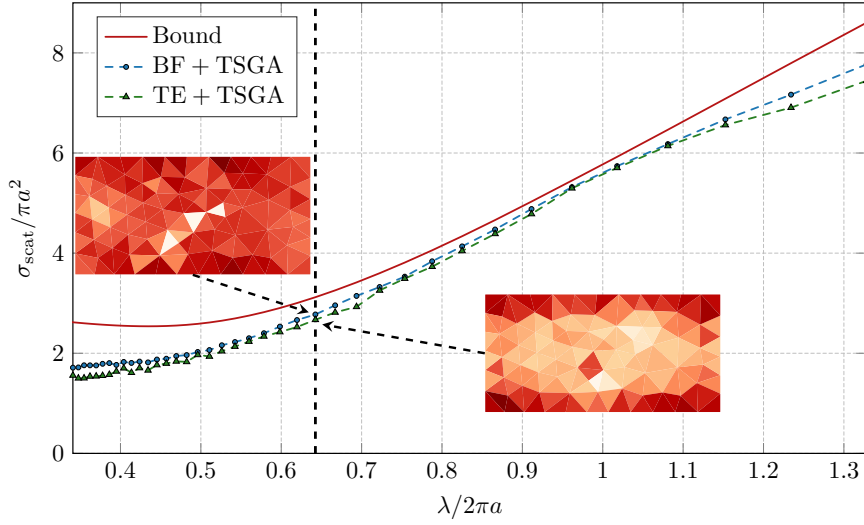
Figure 5.10: Maximization of scattering cross-section of $2l \times l \times l/5$, $l = 200\,\text{nm}$ slab made of gold [82] at $f \in [160, 624]\,\text{THz}$. The plane wave is polarized along the longer edge of the slab and impinges perpendicularly to it. The slab is discretized into 460 tetrahedra which results in 1380 basis functions. The algorithms with both perturbation schemes, *i.e.*, basis function (BF) and tetrahedra (TE) based algorithms, are compared to the bound. The dashed line presents a particular example of realized shapes, and their current distributions, and some real parameters characterizing the algorithm are presented in table 5.1

	BF+TSGA	**TE+TSGA**
agents / iterations	120 / 200	
degrees of freedom	$N = 1380$	$T = 460$
computation time [s]	1600	900
evaluated shapes	7.1×10^7	2.5×10^7
realized $\sigma_{\text{scat}}/\pi a^2$	2.77	2.67

Table 5.1: The complexity of developed algorithm maximizing scattering cross section (5.11) of a slab made of gold at frequency $f = 3.31\,\text{THz}$, see dashed line in figure 5.10. The comparison between basis function (BF) and tetrahedral (TE) based perturbation scheme for the algorithm.

1. Ground plane with dimensions $3\,\text{mm} \times 60\,\text{mm} \times 120$ mm.

2. Feeding stub of height $10\,\text{mm}$.

3. N-connector with inner diameter $7\,\text{mm}$ and outer diameter $3.04\,\text{mm}$.

4. Antenna motive etched into a copper cladding with thickness $35\,\mu\text{m}$ placed on a dielectric slab with relative permittivity $\varepsilon_{\text{r}} = 3$ and thickness $1\,\text{mm}$.

Three designs were collected across the class and will further be used as a comparison to the design proposed by the developed topology sensitivity

algorithm. The performance of collected designs, *i.e.*, parameter $|S_{11}|$, is depicted in figure 5.11. All students approached the design in similar manner trying to design L-shaped PIFA [84], where the top patch consists of two separate current paths for both frequency bands. Since the set of design variables (length of L-slot, etc.) is small, the goal was to satisfy $|S_{11}| < -12\,\text{dB}$ only for middle frequencies of both bands. Figure 5.11 illustrates that good matching is acquired only in one of the two bands. Furthermore, only the red-line design is considered as counter example of human-powered design to developed optimization algorithm, since it satisfies reasonable matching in both bands. This last design is also manufactured and measured, see red curve in figure 5.14. Frequency shift in the DCS band is probably caused by improper simulation model, since, the top conductive patch is not realized on a dielectric substrate, but by copper slab.
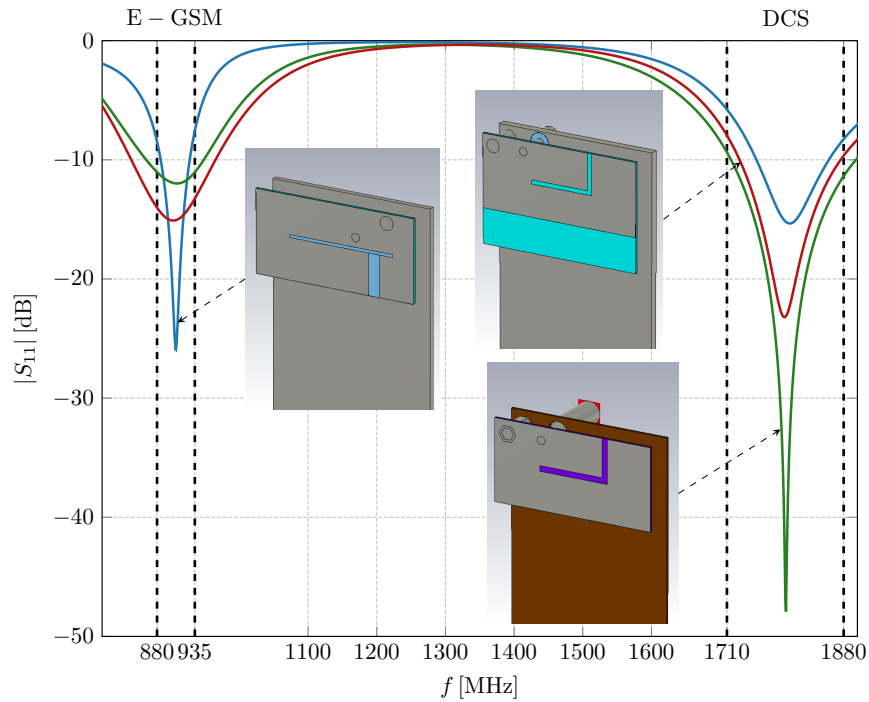
Figure 5.11: Three designs of PIFA made in CST studio collected across the class and their performance in terms of reflectance $|S_{11}|$.

PIFA was also optimized via the developed memetic algorithm to obtain an optimal shape in terms of minimal reflection $|S_{11}|$. As opposed to the previous design, we do not emphasize a goal in terms of a particular number, but in terms of the achievement of $|S_{11}|$ as minimal as possible. In order to control shape's regularity, geometrical constraints are involved in the

optimization task, which reads

$$
\begin{aligned}
\min_{\mathbf{t}_i} \quad & \sum_{n=1}^{N_f} |S_{11}|_n \left(1 + \alpha A_{\text{rel}}(\mathbf{t}_i)\right)\left(1 + \beta h(\mathbf{t}_i)\right) \\
\text{s.t.} \quad & \mathbf{I}(\mathbf{g}_i) = \mathbf{Z}(\mathbf{g}_i)^{-1}\mathbf{V}, \\
& \mathbf{g}_i = \neg \mathcal{B}\left(\mathbf{M}^{\mathrm{T}}\mathbf{t}_i - 2\right), \\
& \mathbf{t}_i \in \{0,1\}^N.
\end{aligned}
\tag{5.12}
$$

Since the PIFA is optimized within SMoM paradigm, we assume infinitesimally thin plates made of PEC and no dielectrics involved. This initial shape of PIFA was modelled in AToM and discretized into 1240 triangles and 1804 basis functions. The shape was split into two regions: controllable region (293 triangles), where the algorithm can perform triangular perturbation, and fixed region, where the algorithm cannot alter the shape, see figure 5.12. A region close to the feeding stub is also considered to be fixed in order to provide unbiased current distribution around the feeding.
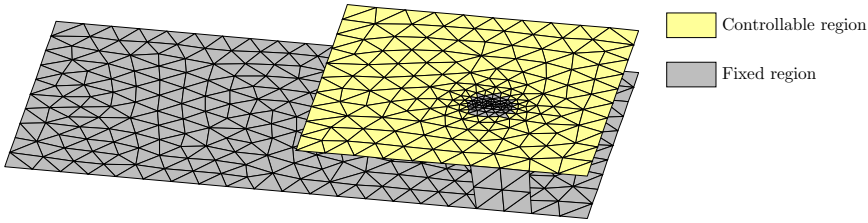
Figure 5.12: Discretized model of PIFA exported from AToM. Model is split into two regions. Structural perturbation is performed by the algorithm only in the controllable region.

The model was optimized to minimize reflection $|S_{11}|$ not only at the middle frequencies of both bands but also at sides of each band, *i.e.*, $N_f = 6$ in (5.12). The constants α and β, weighting the geometrical metrics, are chosen to be 0.2 and 0.4, respectively. The controllable region was optimized by the implemented memetic algorithm with 120 agents and 400 iterations. The computation was performed on RCI computer cluster and took 266 minutes.

The resulting shape was also modelled in CST to receive a more realistic design since the design optimized by the memetic algorithm was obtained under a few assumptions, *e.g.*, infinitesimally small thickness of metal or no dielectrics involved. Nevertheless, the top patch of PIFA is often etched onto a dielectric substrate. Therefore, a model transferred into CST requires an additional post-processing technique in order to tune the design's $|S_{11}|$. The top patch is realized on dielectric substrate IS400 [79] of thickness 0.51 mm with $\varepsilon_r = 3.9$. The metallization is realized by copper folio of thickness 35 μm. Both original and CST designs are summarized in terms of parameter $|S_{11}|$ in figure 5.13.

The post-processed model is further manufactured, see figure 5.14, and measured in an anechoic chamber in order to get rid of unwanted reflections.

The comparison of obtained designs and measured manufactured antenna in terms of performance is depicted in figure 5.14 and compared to the human-powered design described earlier.
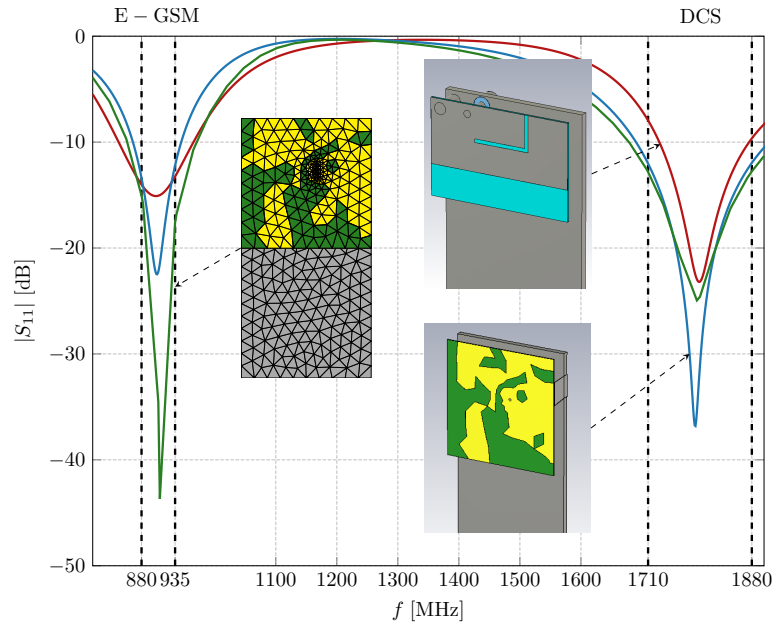
Figure 5.13: Comparison of reflectance $|S_{11}|$ for human-powered design (red), an optimal shape obtained by the developed algorithm (green) and optimal shape transferred to CST Studio Suite (blue) in order to obtain manufacturable design (finite thickness of metallization, dielectrics, etc.).
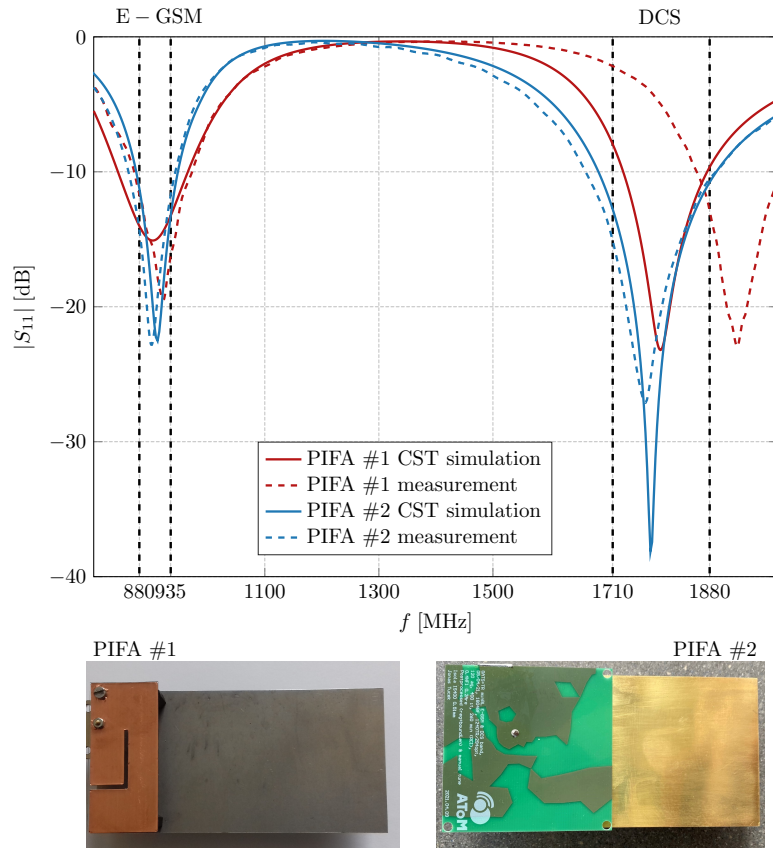
Figure 5.14: Comparison of reflectance $|S_{11}|$ of manufactured PIFA designs obtained by human design (red) and topology sensitivity algorithm (blue). The designs are simulated in CST Studio Suite and compared with manufactured antennas, see photos.

Chapter 6

Conclusion

The topology sensitivity algorithm based on exact re-analysis with block perturbation scheme was implemented for surface and volumetric electromagnetic structures. The algorithm is defined within method of moments paradigm with triangular and tetrahedral discretization with RWG and piece-wise constant basis functions, respectively. The local step employs inversion-free formulas to avoid repetitive matrix inversions and approximates topology gradient by finite differences. The original formulation of the topology sensitivity algorithm based on basis functions is associated with the interpretation issue of geometrical modification. The issue is handled by implementing a mesh element perturbation scheme since a mesh element removal is directly interpreted in geometrical alteration.

The local step is combined with a genetic algorithm to form a memetic framework which is implemented in MATLAB. The inversion-free formulas for the topology sensitivity evaluation of each possible mesh element modification are vectorized, greatly reducing computational time compared to a code based on scripted loops.

The developed procedure was applied to several optimization problems to prove its efficiency in the field of antenna synthesis. The implemented algorithm was compared with the original version based on perturbation of basis functions. The performance was also compared with the known realizations found via adjoint formulation of topology optimization. The developed algorithm was also compared to a human-powered antenna synthesis. Two designs covered in examples were manufactured.

It was proven that the topology sensitivity algorithm operating over mesh elements is more efficient in terms of computational time for large-scale structures rather than an algorithm operating over basis functions. Combination with geometrical metrics results in more easily manufactured designs since a mesh element removal is easily geometrically interpreted. Nevertheless, the reduction of solution space most likely results in optimized metrics being further from the bound.

The developed algorithm can be enhanced in many ways, and it will be the topic of future work.

6.1 Future work

Future work will aim at deepening our knowledge of antenna synthesis with the topology sensitivity algorithm. Achievable details in the structure are limited due to the fixed discretization. Therefore, the obtained designs require re-meshing and re-optimization in order to reach structural convergence. Performing adaptive re-meshing of a locally optimal shape, *e.g.*, mapping to finer mesh after each iteration, see (A) and (B) in figure 6.1, would be a great enhancement for the algorithm. Furthermore, optimization of structures discretized in a different manner, *e.g.*, equilateral triangular discretization, see (C) in figure 6.1, may result in designs being more conforming with the task and also may result in physical quantities being closer to the bound.

In this thesis, two possible structural modifications (basis functions, mesh elements) were considered. However, arbitrary large structural modification, *e.g.*, two mesh elements, may be employed, which will result in optimizing a cheap model, which can provide an initial shape for the consequent optimization process.

In this thesis, a mesh element was subjected to binary optimization. Nevertheless, arbitrary material can be assigned to a mesh element, modifying the binary optimization to general multi-state integer optimization, enlarging the solution space.

Even though the optimization process was accelerated by introducing inversion-free formulas, it is still considered to be a high computational burden. An introduction of symmetries into the optimized model, see (D) in figure 6.1, will reduce the number of unknown and also guarantees geometrical symmetry in the final design.

Genetic operators employed in this thesis were fixed and the same for all optimization tasks. However, their settings can be modified based on the locally optimal shape in each iteration to be more conforming with the local step. Furthermore, several other global algorithms, *e.g.*, particle swarm optimization, may also be more compatible and more efficient with the developed local step.

Simultaneous optimization of multiple metrics requires aggregation of them with given weights. However, to reveal the true trade-off between all the parameters and to do it effectively, they should be optimized in a multi-objective sense.

Future work will also aim at the optimization of designs in nanophotonics and comparison of their performance with those found with a standard tool in the field, which is the adjoint formulation of topology optimization.

Simplifying assumptions within the optimization process, *e.g.*, infinitely thin metallization or no dielectrics involved, negatively affect a resulting design if it is further manufactured. Therefore, the design requires manual tuning in a common EM-simulator to obtain a manufacturable model. It would be more convenient and certainly is a future topic to introduce dielectrics into the optimization process since the most accurate manufacturing processes are based on etching the conductive material onto a dielectric substrate.
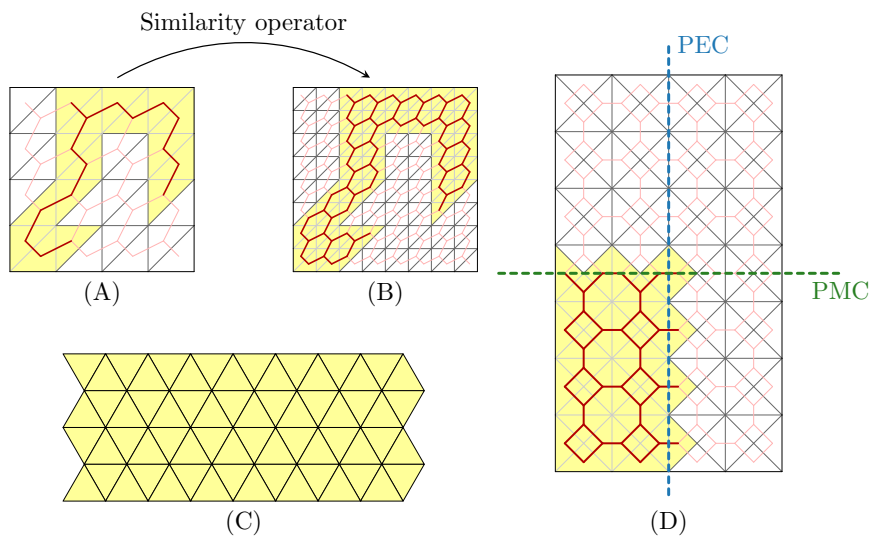
Figure 6.1: Mapping of a shape (A) onto a finer mesh (B). Different kind of triangular discretization (C) for the optimization which can result in an optimal shape with better geometrical and physical performance than discretization used in this thesis. Introduction of symmetries, *e.g.*, perfect electric or magnetic conductor (PEC or PMC), can significantly reduce degrees of freedom for the optimization, thus, computational time.

Appendix **A**

Bibliography

[1] (Feb. 2019) Cisco Visual Networking Index. CISCO. Accessed on 01/04/2021. [Online]. Available: https://s3.amazonaws.com/media.mediapost.com/uploads/CiscoForecast.pdf

[2] C. A. Balanis, *Antenna Theory Analysis and Design*, 3rd ed. Wiley, 2005.

[3] R. Garg, *Analytical and Computational Methods in Electromagnetics*. Artech House, 2008.

[4] Altair. (2020) FEKO. Altair. [Online]. Available: https://www.altair.com/feko/

[5] (2020) CST Studio Suite. Dassault Systemes. [Online]. Available: https://www.3ds.com/products-services/simulia/products/cst-studio-suite/

[6] T. H. Cormen, C. E. Leiserson, R. L. Rivest, and C. Stein, *Introduction to Algorithms*, 3rd ed. Massachusetts Institute of Technology, 2009.

[7] M.-Y. Kao, Ed., *Encyclopedia of Algorithms*. Springer, 2008.

[8] S. Boyd and L. Vandenberghe, *Convex Optimization*. Cambridge, Great Britain: Cambridge University Press, 2004.

[9] E. Lawler, *Combinatorial Optimization: Networks and Matroids*. Mineola, New York, United States: Dover, 2011.

[10] S. Koziel and S. Ogurtsov, *Antenna design by simulation-driven optimization*. Springer, 2014.

[11] M. P. Bendsoe and O. Sigmund, *Topology Optimization*, 2nd ed. Berlin, Germany: Springer, 2004.

[12] M. Capek, L. Jelinek, and M. Gustafsson, "Inversion-free evaluation of nearest neighbors in method of moments," 2019, in press (AWPL).

[13] Y. Rahmat-Samii and E. Michielssen, Eds., *Electromagnetic Optimization by Genetic Algorithms*. Wiley, 1999.

[14] R. F. Harrington, *Field Computation by Moment Methods.* Piscataway, New Jersey, United States: Wiley – IEEE Press, 1993.

[15] M. N. O. Sadiku, *Numerical Techniques in Electromagnetics with Matlab*, 3rd ed. CRC Press, 2009.

[16] J. L. Volakis, A. Chatterjee, and L. C. Kempel, *Finite Element Method Electromagnetics: Antennas, Microwave Circuits, and Scattering Applications.* Wiley – IEEE Press, 1998.

[17] S. M. Rao and D. R. Wilton, "Transient scattering by conducting surfaces of arbitrary shape," *IEEE Transactions on Antennas and Propagation*, vol. 39, no. 1, pp. 56–61, 1991.

[18] K. Deb, *Multi-Objective Optimization using Evolutionary Algorithms.* New York, United States: Wiley, 2001.

[19] W. C. Chew, M. S. Tong, and B. Hu, *Integral Equation Methods for Electromagnetic and Elastic Waves.* Morgan & Claypool, 2009.

[20] R. F. Harrington, *Time-Harmonic Electromagnetic Fields*, 2nd ed. Wiley – IEEE Press, 2001.

[21] W. C. Gibson, *The Method of Moments in Electromagnetics*, 2nd ed. Chapman and Hall/CRC, 2014.

[22] J. D. Jackson, *Classical Electrodynamics*, 3rd ed. Wiley, 1998.

[23] W. C. Chew, *Waves and Fields in Inhomogeneous Media.* IEEE Press, 1995.

[24] L. Jelinek and M. Capek, "Optimal currents on arbitrarily shaped surfaces," *IEEE Trans. Antennas Propag.*, vol. 65, no. 1, pp. 329–341, Jan. 2017.

[25] G. L. Nemhauser and L. A. Wolsey, *Integer an Combinatorial Optimization.* John Wiley & Sons, 1999.

[26] R. L. Haupt and D. H. Werner, *Genetic Algorithms in Electromagnetics.* John Wiley & Sons, 2007.

[27] J. Kennedy and R. Eberhart, "Particle swarm optimization," in *IEEE International Conference on Neural Networks*, vol. 4, Nov. 1995, pp. 1942–1948.

[28] D. Whitley, "A genetic algorithm tutorial," *Statistics and computing*, vol. 4, no. 2, pp. 65–85, 1994.

[29] P. Moscato, C. Cotta, and A. Mendes, "Memetic algorithms," in *New optimization techniques in engineering.* Springer, 2004, pp. 53–85.

[30] O. Sigmund, "On the usefulness of non-gradient approaches in topology optimization," *Struct. Multidisc. Optim.*, vol. 43, pp. 589–596, 2011.

[31] S. Koziel and S. Ogurtsov, "Simulation-driven design in microwave engineering: methods," in *Computational Optimization, Methods and Algorithms.* Springer, 2011, pp. 153–178.

[32] S. Koziel, J. W. Bandler, and K. Madsen, "A space-mapping framework for engineering optimization—theory and implementation," *IEEE Transactions on Microwave Theory and Techniques*, vol. 54, no. 10, pp. 3721–3730, 2006.

[33] J. S. Dokken, S. W. Funke, A. Johansson, and S. Schmidt, "Shape optimization using the finite element method on multiple meshes with nitsche coupling," *SIAM Journal on Scientific Computing*, vol. 41, no. 3, pp. A1923–A1948, 2019.

[34] J. J. Reuther, A. Jameson, J. J. Alonso, M. J. Rimllnger, and D. Saunders, "Constrained multipoint aerodynamic shape optimization using an adjoint formulation and parallel computers, part 2," *Journal of aircraft*, vol. 36, no. 1, pp. 61–74, 1999.

[35] S. Schmidt, E. Wadbro, and M. Berggren, "Large-scale three-dimensional acoustic horn optimization," *SIAM Journal on Scientific Computing*, vol. 38, no. 6, pp. B917–B940, 2016.

[36] C. M. Lalau-Keraly, S. Bhargava, O. D. Miller, and E. Yablonovitch, "Adjoint shape optimization applied to electromagnetic design," *Optics express*, vol. 21, no. 18, pp. 21 693–21 701, 2013.

[37] M. P. Bendsoe and N. Kikuchi, "Generating optimal topologies in structural design using a homogenization method," 1988.

[38] P. I. Borel, A. Harpøth, L. H. Frandsen, M. Kristensen, P. Shi, J. S. Jensen, and O. Sigmund, "Topology optimization and fabrication of photonic crystal structures," *Optics express*, vol. 12, no. 9, pp. 1996–2001, 2004.

[39] R. E. Christiansen and O. Sigmund, "A tutorial for inverse design in photonics by topology optimization," *arXiv preprint arXiv:2008.11816*, 2020.

[40] A. R. Diaz and O. Sigmund, "A topology optimization method for design of negative permeability metamaterials," *Structural and Multidisciplinary Optimization*, vol. 41, no. 2, pp. 163–177, 2010.

[41] A. Erentok and O. Sigmund, "Topology optimization of sub-wavelength antennas," *IEEE Trans. Antennas Propag.*, vol. 59, no. 1, pp. 58–69, 2011.

[42] J. K. Guest, J. H. Prévost, and T. Belytschko, "Achieving minimum length scale in topology optimization using nodal design variables and projection functions," *International journal for numerical methods in engineering*, vol. 61, no. 2, pp. 238–254, 2004.

[43] S. Liu, Q. Wang, and R. Gao, "A topology optimization method for design of small gpr antennas," *Structural and Multidisciplinary Optimization*, vol. 50, no. 6, pp. 1165–1174, 2014.

[44] ——, "MoM-based topology optimization method for planar metallic antenna design," *Acta Mechanica Sinica*, vol. 32, no. 6, pp. 1058–1064, Dec. 2016.

[45] Q. Wang, R. Gao, and S. Liu, "A novel parameterization method for the topology optimization of metallic antenna design," *Acta Mechanica Sinica*, vol. 33, no. 6, pp. 1040–1050, 2017.

[46] M. Capek, P. Hazdra, M. Mazanek, Z. Raida, and J. Rymus, "The antenna toolbox for matlab (atom)," in *Proceedings of the 9th European Conference on Antennas and Propagation (EUCAP)*, Lisbon, Portugal, July 2015.

[47] M. Capek, L. Jelinek, and M. Gustafsson, "Shape synthesis based on topology sensitivity," *IEEE Trans. Antennas Propag.*, vol. 67, no. 6, pp. 3889 – 3901, June 2019.

[48] M. Ohsaki, *Optimization of finite dimensional structures.* CRC Press, 2016.

[49] W. W. Hager, "Updating the inverse of a matrix," *SIAM Review*, vol. 31, pp. 221–239, 1989.

[50] A. D. Yaghjian and S. R. Best, "Impedance, bandwidth and Q of antennas," *IEEE Trans. Antennas Propag.*, vol. 53, no. 4, pp. 1298–1324, Apr. 2005.

[51] G. A. E. Vandenbosch, "Reactive energies, impedance, and Q factor of radiating structures," *IEEE Trans. Antennas Propag.*, vol. 58, no. 4, pp. 1112–1127, Apr. 2010.

[52] C. A. Balanis, *Advanced Engineering Electromagnetics.* Wiley, 1989.

[53] S. M. Rao, D. R. Wilton, and A. W. Glisson, "Electromagnetic scattering by surfaces of arbitrary shape," *IEEE Trans. Antennas Propag.*, vol. 30, no. 3, pp. 409–418, May 1982.

[54] A. Polimeridis, J. Villena, L. Daniel, and J. White, "Stable FFT-JVIE solvers for fast analysis of highly inhomogeneous dielectric objects," *Journal of Computational Physics*, vol. 269, pp. 280–296, July 2014. [Online]. Available: https://doi.org/10.1016/j.jcp.2014.03.026

[55] (2019) Antenna Toolbox for MATLAB (AToM). Czech Technical University in Prague. Www.antennatoolbox.com. [Online]. Available: www.antennatoolbox.com

[56] G. H. Golub and C. F. Van Loan, *Matrix Computations.* Johns Hopkins University Press, 2012.

[57] R. J. Lipton and K. W. Regan, "David johnson: Galactic algorithms," in *People, Problems, and Proofs.* Springer, 2013, pp. 109–112.

[58] V. Strassen, "Gaussian elimination is not optimal," *Numerische mathematik*, vol. 13, no. 4, pp. 354–356, 1969.

[59] D. Coppersmith and S. Winograd, "Matrix multiplication via arithmetic progressions," in *Proceedings of the nineteenth annual ACM symposium on Theory of computing*, 1987, pp. 1–6.

[60] B. Bollobás, *Modern graph theory.* Springer Science & Business Media, 2013, vol. 184.

[61] A. F. Peterson, S. L. Ray, and R. Mittra, *Computational Methods for Electromagnetics.* Wiley – IEEE Press, 1998.

[62] M. Van Steen, "Graph theory and complex networks," *An introduction*, vol. 144, 2010.

[63] H. B. Enderton, *A mathematical introduction to logic.* Elsevier, 2001.

[64] D. Schaubert, D. Wilton, and A. Glisson, "A tetrahedral modeling method for electromagnetic scattering by arbitrarily shaped inhomogeneous dielectric bodies," *IEEE Transactions on Antennas and Propagation*, vol. 32, no. 1, pp. 77–85, January 1984. [Online]. Available: https://doi.org/10.1109/tap.1984.1143193

[65] B. Yang and J. J. Adams, "Systematic shape optimization of symmetric mimo antennas using characteristic modes," *IEEE Trans. Antennas Propag.*, vol. 64, no. 7, pp. 2668–2678, July 2016.

[66] M. Capek, V. Neuman, J. Tucek, L. Jelinek, and M. Gustafsson, "Topology optimization of electrically small antennas with shape regularity constraints," in *2021 15th European Conference on Antennas and Propagation (EuCAP).* IEEE, 2021, pp. 1–5.

[67] A. N. Kolmogorov and S. V. Fomin, *Elements of the Theory of Functions and Functional Analysis.* Dover, 1999.

[68] (2018) Vectorization: A key tool to improve performance on modern cpus. [Online]. Available: https://software.intel.com/content/www/us/en/develop/articles/vectorization-a-key-tool-to-improve-performance-on-modern-cpus.html

[69] (2018) The Matlab. The MathWorks. [Online]. Available: www.mathworks.com

[70] F. Neri, C. Cotta, and P. Moscato, *Handbook of memetic algorithms.* Springer, 2011, vol. 379.

[71] M. Gen and R. Cheng, *Genetic algorithms and engineering optimization.* John Wiley & Sons, 1999, vol. 7.

[72] (2017) Fast Optimization Procedures (FOPS). Czech Technical University in Prague. [Online]. Available: www.antennatoolbox.com/fops

[73] (2020) Cluster at Research Center for Informatics (RCI). Czech Technical University in Prague. [Online]. Available: http://rci.cvut.cz

[74] *145-2013 – IEEE Standard for Definitions of Terms for Antennas*, IEEE Std., Mar. 2014.

[75] M. Capek and L. Jelinek, "Optimal composition of modal currents for minimal quality factor Q," *IEEE Trans. Antennas Propag.*, vol. 64, no. 12, pp. 5230–5242, Dec. 2016.

[76] M. Capek, L. Jelinek, K. Schab, M. Gustafsson, B. L. G. Jonsson, F. Ferrero, and C. Ehrenborg, "Optimal planar electric dipole antennas: Searching for antennas reaching the fundamental bounds on selected metrics," vol. 61, no. 4, pp. 19–29, Aug. 2019.

[77] M. Gustafsson, C. Sohl, and G. Kristensson, "Illustrations of new physical bounds on linearly polarized antennas," *IEEE Trans. Antennas Propag.*, vol. 57, no. 5, pp. 1319–1327, May 2009.

[78] R. F. Harrington, "Effect of antenna size on gain, bandwidth, and efficiency," *J. Res. Nat. Bur. Stand.*, vol. 64-D, pp. 1–12, Jan.–Feb. 1960.

[79] *Lead Free, Mid Tg Epoxy Laminate and Prepreg*, Isola, May 2021. [Online]. Available: https://www.isola-group.com/pcb-laminates-prepreg/is400/

[80] F. Frezza, F. Mangini, and N. Tedeschi, "Introduction to electromagnetic scattering: tutorial," *JOSA A*, vol. 35, no. 1, pp. 163–173, 2018.

[81] C. F. Bohren and D. R. Huffman, *Absorption and Scattering of Light by Small Particles.* Wiley, 1983.

[82] A. Derkachova, K. Kolwas, and I. Demchenko, "Dielectric function for gold in plasmonics applications: Size dependence of plasmon resonance frequencies and damping rates for nanospheres," vol. 11, pp. 941–951, 6 2016.

[83] M. Gustafsson, K. Schab, L. Jelinek, and M. Capek, "Upper bounds on absorption and scattering," *New Journal of Physics*, vol. 22, no. 7, p. 073013, 2020.

[84] Z. Zhang, *Antenna design for mobile devices.* John Wiley & Sons, 2017.

[85] R. A. Horn and C. R. Johnson, *Matrix Analysis.* Cambridge, United Kingdom: Cambridge University Press, 2017.

[86] L. Hogben, *Handbook of linear algebra.* CRC press, 2006.

[87] F. Zhang, *Matrix theory: basic results and techniques.* Springer Science & Business Media, 2011.

[88] J. Tuček, *Local Perturbation in Method of Moments.* Czech Technical University in Prague, 2019.

Appendix B
Electric Field Integral Equations

The derivation of electric field integral equation (EFIE) starts from an assumption of incident electric field $\boldsymbol{E}^{\mathrm{i}}$ being scattered by a dielectric or conducting obstacle under time-harmonic steady state at angular frequency ω and convention $\partial/\partial t \to \mathrm{j}\omega$, with j being imaginary unit. In order to solve the scattering problem, let us begin with the vector wave equation

$$\nabla \times \nabla \times \boldsymbol{E} - k^2 \boldsymbol{E} = -\mathrm{j}\omega\mu\boldsymbol{J}, \tag{B.1}$$

where $k = \omega\sqrt{\mu\varepsilon}$ denotes wave-number in material background. Employing common vector identities, Gauss law and charge conservation leads to

$$\nabla^2 \boldsymbol{E} + k^2 \boldsymbol{E} = \mathrm{j}\omega\mu\boldsymbol{J} - \frac{1}{\mathrm{j}\omega\varepsilon}\nabla\nabla \cdot \boldsymbol{J}, \tag{B.2}$$

where current density $\boldsymbol{J}$ aggregates polarization currents in the obstacle $\boldsymbol{J}^{\mathrm{s}}$ as well as current density producing the incident field $\boldsymbol{J}^{\mathrm{i}}$. Since equation (B.2) is linear, a dyadic Green's function [23]

$$\overline{\mathbf{G}}\left(\boldsymbol{r}, \boldsymbol{r}'\right) = \left[\mathbb{I} + \frac{1}{k^2}\nabla\nabla\right]\frac{e^{-\mathrm{j}k|\boldsymbol{r}-\boldsymbol{r}'|}}{4\pi|\boldsymbol{r}-\boldsymbol{r}'|}, \tag{B.3}$$

with $\mathbb{I}$ denoting the unit dyad, can be employed to get [21]

$$\boldsymbol{E}\left(\boldsymbol{r}\right) = \boldsymbol{E}^{\mathrm{i}}\left(\boldsymbol{r}\right) - \mathrm{j}\omega\mu\int_{\Omega'}\overline{\mathbf{G}}\left(\boldsymbol{r}, \boldsymbol{r}'\right) \cdot \boldsymbol{J}^{\mathrm{s}}\left(\boldsymbol{r}'\right)\,\mathrm{d}\boldsymbol{r}'. \tag{B.4}$$

When relation (B.4) is accompanied by a constitutive relation describing the material obstacle $\boldsymbol{r} \in \Omega$ made of resistivity $\rho(\boldsymbol{r})$

$$\boldsymbol{E}(\boldsymbol{r}) = \rho(\boldsymbol{r})\boldsymbol{J}^{\mathrm{s}}(\boldsymbol{r}), \quad \boldsymbol{r} \in \Omega, \tag{B.5}$$

integro-differential equation, known as EFIE, for the unknown current density $\boldsymbol{J}^{\mathrm{s}}$ is formed and reads

$$\boldsymbol{E}^{\mathrm{i}}\left(\boldsymbol{r}\right) = \rho(\boldsymbol{r})\boldsymbol{J}^{\mathrm{s}}\left(\boldsymbol{r}\right) + \mathrm{j}\omega\mu\int_{\Omega'}\overline{\mathbf{G}}\left(\boldsymbol{r}, \boldsymbol{r}'\right) \cdot \boldsymbol{J}^{\mathrm{s}}\left(\boldsymbol{r}'\right)\,\mathrm{d}\boldsymbol{r}', \quad \boldsymbol{r} \in \Omega \tag{B.6}$$

As formulated, the EFIE describes scattering by a penetrable body characterized by electric susceptibility $\chi\left(\boldsymbol{r}\right)$ and the resistivity $\rho^{-1}\left(\boldsymbol{r}\right) = \mathrm{j}\omega\varepsilon_0\chi\left(\boldsymbol{r}\right)$.

The modification to highly conducting scatteres is, however, straightforward. In such a case, the current density is assumed to exist only on the surface of the body and resistivity is replaced by surface impedance $Z_\mathrm{s}\left(\boldsymbol{r}\right)$ [22]. In the surface case, the equation (B.6) is enforced only on the surface of the obstacle.

Appendix C

Method of Moments

Method of moments (MoM) [14] is a mathematical technique for solving operator equation

$$\mathcal{L}(\boldsymbol{f}) = \boldsymbol{g}, \tag{C.1}$$

where $\mathcal{L}$ is a linear operator, $\boldsymbol{g}$ is a known function and $\boldsymbol{f}$ is an unknown vector function. MoM employs an expansion of the unknown function $\boldsymbol{f}$ into a sum of weighted basis functions $\{\boldsymbol{\psi}_n(\boldsymbol{r})\}$

$$\boldsymbol{f} \approx \sum_{n=1}^{N} a_n \boldsymbol{\psi}_n, \tag{C.2}$$

where a_n are unknown weights. The set of basis functions is assumed to be linearly independent and such that for $N \to \infty$ and appropriately chosen weights a_n, the sum (C.2) uniformly converges to the exact solution of (C.1). Due to the assumed linearity of $\mathcal{L}$, substitution of (C.2) into (C.1) yields

$$\sum_{n=1}^{N} a_n \mathcal{L}(\boldsymbol{\psi}_n) = \boldsymbol{g}. \tag{C.3}$$

Next step is the formulation of inner product or moment between a function $\boldsymbol{\psi}_n$ and a testing function $\boldsymbol{w}_m$ as

$$\langle \boldsymbol{w}_m, \boldsymbol{\psi}_n \rangle = \int_{\Omega_m} \boldsymbol{w}_m^* \cdot \boldsymbol{\psi}_n \, \mathrm{d}\boldsymbol{r}_m, \tag{C.4}$$

where * denotes complex conjugate. Testing functions $\boldsymbol{w}_m$ are assumed to be linearly independent. Applying (C.4) on (C.3) using N testing functions, leads to an $N \times N$ system of linear equations. This method is equivalent to Ritz method or, when testing functions and weighting functions are identical, to Galerkin method [21]. In this later case, the system of N equations for N unknown weights a_n reads

$$\sum_{n=1}^{N} a_n \langle \boldsymbol{\psi}_m, \mathcal{L}(\boldsymbol{\psi}_n) \rangle = \langle \boldsymbol{\psi}_m, \boldsymbol{g} \rangle, \quad m = 1, ..., N, \tag{C.5}$$

which can be symbolically reduced to

$$\mathbf{Z}\mathbf{a} = \mathbf{b}. \tag{C.6}$$

Finding suitable basis and testing functions is a crucial task for acquiring desired accuracy and a well-behaved system matrix and heavily depends on the particular operator equation to be solved. In the case of this thesis, the operator equation is EFIE.

In this thesis MoM is employed on volumetric and surface structures forming a set of natural steps:

1. choosing appropriate discretization (triangular, tetrahedral, ...)

2. choosing compatible basis and testing functions (Rao-Wilton-Glisson [53], piece-wise constant [54], ...)

3. filling a system matrix and evaluating the unknown field

4. evaluating unknown state variable **a** by matrix inversion of system matrix

5. visualisation of unknown field inside each discretization element.

■ **C.1 Basis functions**

The electric and magnetic currents on planar geometries are expanded using a sum of weighted basis functions (C.2). The most popular choice of basis functions for modelling surface current distribution are Rao-Wilton-Glisson (RWG) triangular basis functions [53]. RWG function, see figure C.1a, is defined as

$$\boldsymbol{\psi}_n(\boldsymbol{r}) = \begin{cases} \dfrac{l_n}{2A_n^+}\boldsymbol{\rho}_n^+(\boldsymbol{r}) & \boldsymbol{r} \in T_n^+, \\ \dfrac{l_n}{2A_n^-}\boldsymbol{\rho}_n^-(\boldsymbol{r}) & \boldsymbol{r} \in T_n^-, \\ 0 & \text{otherwise}, \end{cases} \tag{C.7}$$

where T_n^+ and T_n^- are two conjoined triangle associated with n-th edge of length l_n. Vectors $\boldsymbol{\rho}_n^+(\boldsymbol{r})$ and $\boldsymbol{\rho}_n^-(\boldsymbol{r})$ point toward the vertex $\boldsymbol{r}_n^+$ and away from the vertex $\boldsymbol{r}_n^-$

$$\boldsymbol{\rho}_n^+(\boldsymbol{r}) = \boldsymbol{r}_n^+ - \boldsymbol{r} \quad \boldsymbol{r} \in T_n^+, \tag{C.8}$$
$$\boldsymbol{\rho}_n^-(\boldsymbol{r}) = \boldsymbol{r} - \boldsymbol{r}_n^- \quad \boldsymbol{r} \in T_n^-. \tag{C.9}$$

These basis functions are assigned only to interior edges shared by two adjacent triangles. Therefore, a triangle can be composed of up to three basis functions. Basis functions with similar properties can be employed on volumetric bodies. Schaubert-Wilton-Glisson (SWG) basis functions [64] can be used. However, in this thesis, we assume utilization of piece-wise constant basis functions with tetrahedral discretization [54].

Each tetrahedral element always contains exactly three basis functions, which is usually chosen to be unit-vectors or triplets $\boldsymbol{\psi}_n(\boldsymbol{r}) = \{\hat{x}, \hat{y}, \hat{z}\}$, see figure C.1b. This choice readily provides conversion of volumetric quadrature to surface integrals.
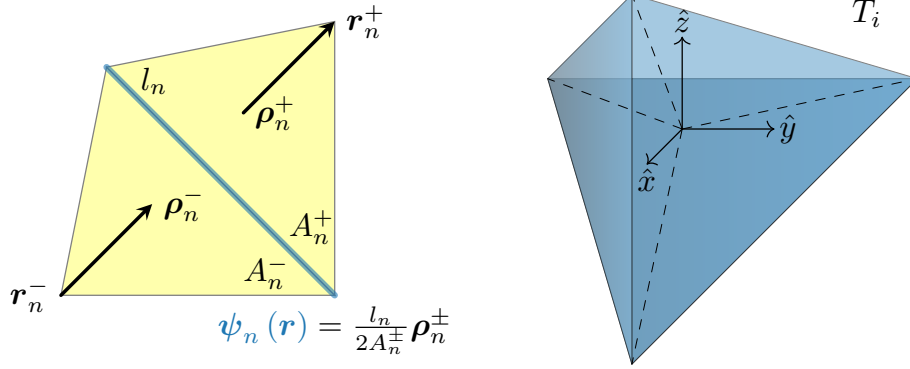
(a) : RWG basis function between two triangluar elements.

(b) : Piece-wise constant basis function on a tetrahedral element.

Figure C.1: Two type of basis functions used in this thesis. RWG basis functions are used to express currents impressed onto planar structures. Piece-wise constant basis functions are used with tetrahedral discretization to determine current distribution in volumetric bodies.

Appendix D

Block matrix inversion

Matrices can be partitioned into blocks, *i.e.*, submatrices. Mathematical operations, *e.g.*, matrix multiplication or inversion, may be defined over them. Properties of block matrices can be found in [85]. Since a row and a column of the impedance matrix represents an electromagnetic interaction between basis functions, the impedance matrix can be partitioned into blocks.

Most fundamental operation for this thesis is a matrix inversion. Let matrix $\mathbf{A}$ be partitioned as

$$\mathbf{A} = \begin{pmatrix} \mathbf{A}_{11} & \mathbf{A}_{12} \\ \mathbf{A}_{21} & \mathbf{A}_{22} \end{pmatrix}, \tag{D.1}$$

where $\mathbf{A}_{ii}$, $i = 1, 2$, are submatrices. An inversion formula for the corresponding blocks of the block matrix $\mathbf{A}^{-1}$ [86] is

$$\begin{pmatrix} \mathbf{A}_{11} & \mathbf{A}_{12} \\ \mathbf{A}_{21} & \mathbf{A}_{22} \end{pmatrix}^{-1} = \begin{pmatrix} \mathbf{A}_{11}^{-1} + \mathbf{A}_{11}^{-1}\mathbf{A}_{12}\mathbf{S}_{\mathbf{A}_{11}}^{-1}\mathbf{A}_{21}\mathbf{A}_{11}^{-1} & -\mathbf{A}_{11}^{-1}\mathbf{A}_{12}\mathbf{S}_{\mathbf{A}_{11}}^{-1} \\ -\mathbf{S}_{\mathbf{A}_{11}}^{-1}\mathbf{A}_{21}\mathbf{A}_{11}^{-1} & \mathbf{S}_{\mathbf{A}_{11}}^{-1} \end{pmatrix}, \tag{D.2}$$

or equivalently

$$\begin{pmatrix} \mathbf{A}_{11} & \mathbf{A}_{12} \\ \mathbf{A}_{21} & \mathbf{A}_{22} \end{pmatrix}^{-1} = \begin{pmatrix} \mathbf{S}_{\mathbf{A}_{22}}^{-1} & -\mathbf{S}_{\mathbf{A}_{22}}^{-1}\mathbf{A}_{12}\mathbf{A}_{22}^{-1} \\ -\mathbf{A}_{22}^{-1}\mathbf{A}_{21}\mathbf{S}_{\mathbf{A}_{22}}^{-1} & \mathbf{A}_{22}^{-1} + \mathbf{A}_{22}^{-1}\mathbf{A}_{21}\mathbf{S}_{\mathbf{A}_{22}}^{-1}\mathbf{A}_{12}\mathbf{A}_{22}^{-1} \end{pmatrix}, \tag{D.3}$$

where $\mathbf{S}_{\mathbf{A}_{11}} = \mathbf{A}_{22} - \mathbf{A}_{21}\mathbf{A}_{11}^{-1}\mathbf{A}_{12}$ and $\mathbf{S}_{\mathbf{A}_{22}} = \mathbf{A}_{11} - \mathbf{A}_{12}\mathbf{A}_{22}^{-1}\mathbf{A}_{21}$ are Schur complements of $\mathbf{A}_{11}$ and $\mathbf{A}_{22}$ [86], respectively.

If and only if both the matrix $\mathbf{A}_{11}$ and the Schur complement $\mathbf{S}$ are nonsingular, then $\mathbf{A}$ is nonsingular [87]. The formula (D.2) is efficient for a known matrix $\mathbf{A}_{11}^{-1}$ and sufficiently small blocks $\mathbf{A}_{12}$, $\mathbf{A}_{21}$, $\mathbf{A}_{22}$ as compared to full inversion of matrix $\mathbf{A}$.

Equating the first element of (D.2) and (D.3) leads to

$$\mathbf{A}_{\text{pert}}^{-1} = \mathbf{A}_{11}^{-1} + \mathbf{A}_{11}^{-1}\mathbf{A}_{12}(\mathbf{A}_{11} - \mathbf{A}_{12}\mathbf{A}_{22}^{-1}\mathbf{A}_{21})^{-1}\mathbf{A}_{21}\mathbf{A}_{11}^{-1}, \tag{D.4}$$

where $\mathbf{A}_{\text{pert}} = \mathbf{A}_{11} - \mathbf{A}_{12}\mathbf{A}_{22}^{-1}\mathbf{A}_{21}$. Equation (D.4) is the Shermann-Morrison-Woodbury formula (SMW) [49]. SMW expresses the inversion of a matrix after a modification in terms of the inversion of the original matrix. If $\mathbf{A}_{11}$ is

71

much bigger than $\mathbf{A}_{22}$, then $\mathbf{A}_{22}$ and $\mathbf{A}_{11} - \mathbf{A}_{12}\mathbf{A}_{22}^{-1}\mathbf{A}_{21}$ are inverted with less computational time than $\mathbf{A}_{\text{pert}}$ [88]. SMW formula is widely applied on the field of statistics, asymptotic analysis or optimization [49].